

# Electronic and Interfacial Properties of 2D MXene/blue phosphorene Heterostructures: Impact of External Strain for Thermoelectric Applications

Sarga P K, Karthik H J, and Swastibrata Bhattacharyya\*

*Department of Physics, Birla Institute of Technology and Science Pilani, K. K. Birla Goa  
Campus, Zuarinagar, Goa, 403726, India*

E-mail: [swastibratab@goa.bits-pilani.ac.in](mailto:swastibratab@goa.bits-pilani.ac.in)

## Abstract

Building two-dimensional (2D) van der Waals (vdW) heterostructures and enhancing their properties through strain engineering unlocks new applications for their constituent materials. In this study, we present a comprehensive first-principles investigation of oxygen-functionalized MXene-based heterostructures ( $M_2CO_2$  ( $M=Sc,Zr,Hf$ )/blue phosphorene), emphasizing their structural, electronic, and thermoelectric properties under the application of various types of strain. Our results indicate a reduction in band gap under strain and metallic transition for in-plane strain (uni- and biaxial strain). Transition from type-I to type-II could be obtained for  $Hf_2CO_2$ /blueP and  $Zr_2CO_2$ /blueP heterostructure by applying strain, providing a method for their potential application in photocatalytic devices that require type-II band alignment for photogenerated charge separation. We observe a positive correlation between strain and thermoelectric efficiency under most conditions, with a significant enhancement

in thermoelectric power factor (PF) and electronic figure of merit ( $ZT_e$ ) achievable in all heterostructures through strain engineering. Among the three heterostructures,  $\text{Sc}_2\text{CO}_2/\text{blueP}$  showed the maximum PF ( $ZT_e$ ) of  $11.2 \times 10^{11} \text{ W/mK}^2\text{s}$  (43.2) for 2% normal compressive (4% biaxial compressive) strain. These findings suggest that MXene/blueP heterostructures hold significant promise for applications in optoelectronics and high-temperature thermoelectric devices.

**keywords** : 2D materials, vdW heterostructure, Structural and electronic properties, Strain engineering, Modulation of electronic properties, Thermoelectric application, First-principles calculations.

## 1 INTRODUCTION

After the successful extraction of graphene from graphite using a mechanical exfoliation method,<sup>1</sup> research into two-dimensional (2D) materials with unique electrical and optical properties has flourished. When it comes to materials science, chemistry, nanoscience, optics, and other subjects, 2D materials shine<sup>2,3</sup> due to their unique properties driven by their dimension compared to their bulk form. Different 2D materials, including graphene, transition metal dichalcogenides (TMDCs), MXene, hexagonal BN (h-BN), and phosphorene are attracting greater attention. MXenes are a new class of 2D transition-metal carbides/carbonitrides/nitrides/borides. Due to their wide range of appealing features, these materials have exhibited considerable potential in many applications such as batteries, capacitors, and electrocatalysis.<sup>4-6</sup> MXenes are derived from MAX phases through etching of the weakly bonded "A" layer. MAX phases are thermodynamically stable, layered hexagonal materials with the general formula  $\text{M}_{n+1}\text{AX}_n$  ( $n=1,2, \text{ or } 3$ ), where "M" is an early transition metal (Ti, Sc, Hf, Zr, V, Nb, Ta, Cr, or Mo), "A" is an A-group element (mostly groups 13 and 14), and "X" is carbon and/or nitrogen.<sup>7</sup> Similar to their bulk counterparts, MXene monolayers ( $\text{M}_{n+1}\text{X}_n$ ) exhibit common properties like metallicity, high selectivity to

intercalants, and a high elastic constant ( $c_{11}$ ). However, their metallic nature and lack of bandgap limit their application in semiconducting and optical nanodevices.<sup>8</sup> In the chemical etching processes, various functional groups (F, OH, O, or H) attached to both sides of the MXene surface, resulting in  $M_{n+1}X_nT_x$ , where  $T_x$  represents the terminating groups. While majority of the functionalized MXenes remain metallic, six members exhibit semiconducting behavior with bandgap values ranging from 0.24 to 1.8 eV:  $Ti_2CO_2$ ,  $Zr_2CO_2$ ,  $Hf_2CO_2$ ,  $Sc_2CO_2$ ,  $Sc_2C(OH)_2$ , and  $Sc_2CF_2$ .<sup>9</sup>

To broaden the use of 2D materials, their properties can be further modified by forming heterostructures. Van der Waals (vdW) heterostructures, which involve vertically stacking two different 2D materials bound by weak vdW interactions, are attracting significant attention. Their distinctive features include an extensive interface area between the constituent materials, atomic-level thinness, and the absence of dangling bonds, highlighting their unique attributes.<sup>10</sup> The interlayer quantum coupling in 2D heterostructures gives rise to new fascinating phenomena, which will lead to revolutionary electronics and optical applications, such as tunneling and bipolar transistors,<sup>11,12</sup> as well as flexible optoelectronic devices.<sup>13</sup> Semiconducting heterostructures are categorized based on their band alignments into three types: type-I, type-II, and type-III.<sup>14</sup> In type-I heterostructures, the valence band maximum (VBM) and the conduction band minimum (CBM) reside in the same layer. Type-II heterostructures (staggered gap) have the CBM and VBM in different monolayers, whereas type-III heterostructures (broken gap) exhibit no band gap.<sup>15</sup> Heterostructures offer new ways to combine the good qualities of the materials they are made of.<sup>16–19</sup> Researchers are particularly interested in semiconducting heterostructures due to their intriguing electronic structures and optical properties, which are promising for applications in photocatalysis, photovoltaics, and optoelectronics. The type-II heterostructures have demonstrated utility in light detection and harvesting applications.<sup>20,21</sup> Such band alignment substantially enhances electron-hole separation efficiencies while concurrently diminishing charge recombination probabilities, thus highly desirable for photovoltaic and photocatalytic devices.<sup>22</sup>

Forming heterostructures enhances mechanical, electronic, optical and thermoelectric properties of MXenes. By combining MXenes with monolayers of other 2D materials, adhering to a lattice parameter mismatch criterion of less than 5%, substantial improvements can be achieved. Notably, the formation of the MXene/TiO<sub>2</sub><sup>23</sup> interface, characterized by substantial charge transfer and strong adhesion, offers valuable insights for customizing these structures to meet specific needs in electrical energy storage applications. Furthermore, the MXene/Graphene heterostructure enhances electrical conductivity, Li adsorption, and mechanical stiffness,<sup>24</sup> while MXene/TMDs heterostructures show promise for gas sensors detecting toxic gases.<sup>25</sup>

Single-layer buckled blue phosphorene (blueP) having a flatter layer than puckered black phosphorene (BlackP), has attracted intense research interest<sup>26</sup> due to exceptional qualities, including sizable bandgap and ultra-high mobility. The electronic and magnetic properties of blueP are highly sensitive to foreign adatoms. For instance, a spin-gapless semiconducting state can result from Co and Ag adatoms, while a half-metallic state can be achieved through the adsorption of N and P.<sup>27</sup> Band gap engineering of blueP under external strain and electric fields is of great interest for applications in nanoelectronics and rechargeable Li-ion batteries.<sup>28</sup> Due to their similar crystal structure and comparable lattice constant, blueP is an excellent material to practically construct vdW heterostructures with 2D M<sub>2</sub>CO<sub>2</sub> (M= Sc,Zr,Hf). Various combinations of MXene/blueP heterostructures have been designed theoretically and studied for applications such as water-splitting photocatalysts<sup>29</sup> and as electrode materials for metal ion batteries.<sup>30</sup> Enhanced optical absorption has been reported in blueP/Sc<sub>2</sub>CX<sub>2</sub> (X= O, F, OH) vdW heterostructures compared to their parent materials, indicating their potential for optoelectronics and photovoltaic device applications.<sup>31</sup>

For the integration of these heterostructures in devices, it is crucial to understand their charge transfer as well as the mechanical stability and tunability of their materials properties under biaxial and uniaxial strain along different direction. Biaxial strain, for instance, applies

uniform stress in two dimensions while uniaxial strain, on the other hand, applies stress along a single direction, enabling the manipulation of material anisotropy, bandgap and electronic states, crucial for nanoelectronics and optoelectronic applications. A theoretical study on  $\text{Zr}_2\text{CO}_2/\text{blueP}$  and  $\text{Hf}_2\text{CO}_2/\text{blueP}$  heterostructures have shown type-I to type-II transition under biaxial strain.<sup>32</sup> Their findings show that the maximum biaxial strains that can be sustained are 0.16 for blueP, 0.18 for  $\text{Zr}_2\text{CO}_2$ , 0.19 for  $\text{Hf}_2\text{CO}_2$ , 0.16 for  $\text{Zr}_2\text{CO}_2/\text{blueP}$ , and 0.17 for  $\text{Hf}_2\text{CO}_2/\text{blueP}$ . Since type-I heterostructures are quite common,<sup>15</sup> this transition to type-II is significant for the design and application of optoelectronic devices.<sup>33</sup>

Many 2D materials show potential applications as thermoelectric (TE) materials offering a promising avenue for converting waste heat into electricity.<sup>34,35</sup> Thermoelectric generators have become very important devices as we navigate rapid technological advancements and have been facing energy challenges. With applications spanning decades in aerospace and automotive sectors, particularly in high-temperature environments,<sup>36</sup> TE generators have garnered substantial interest. Their recent integration into wearable electronics<sup>37</sup> underscores their expanding utility. The application of strain to enhance the power factor and figure of merit ( $ZT_e$ ) of various materials has been well-documented.<sup>38,39</sup> MXenes are emerging as promising candidates for thermoelectric applications due to their cost-effectiveness, environmental benignity, and potential for high activity.<sup>40</sup> BlueP possesses a moderate band gap, lower effective mass, and thereby high carrier mobility, which in turn contributes to an elevated Seebeck coefficient and enhanced electrical conductivity.<sup>41</sup> Since heterostructure combinations have the potential to enhance charge carrier separation and reduce recombination, it is important to investigate the thermoelectric properties of MXene-blueP heterostructures in detail under strain for their application in TE devices.

In this investigation, employing first-principles calculations, we predict optimized stacking and geometries of three MXene/blueP heterostructures i.e.,  $\text{Hf}_2\text{CO}_2/\text{blueP}$ ,  $\text{Zr}_2\text{CO}_2/\text{blueP}$  and  $\text{Sc}_2\text{CO}_2/\text{blueP}$  and present in details about their electronic properties, charge redistri-

bution and stability. We extend our investigation to the profound influence of strain (biaxial and uniaxial strain) on the intrinsic properties of the  $M_2CO_2$  (M= Sc,Zr,Hf)/blueP heterostructures. Given that strain has previously demonstrated its capacity to augment the thermoelectric performance of materials, we have conducted calculations on various thermoelectric coefficients, focusing on enhancing the power factor. Our findings will be helpful for researchers and device engineers to apply these materials for applications in various devices.

## 2 COMPUTATIONAL DETAILS

In this work, all the calculations were executed utilizing *ab initio* Density Functional Theory (DFT) in conjunction with all-electron projected augmented wave potentials (PAW).<sup>42</sup> The Perdew-Burke-Ernzerhof generalized gradient approximation (PBE-GGA)<sup>43</sup> was employed for electronic exchange and correlation, as incorporated within the Vienna *Ab initio* Simulation Package (VASP)<sup>44</sup> with periodic boundary conditions. The optB88-vdW functional<sup>45</sup> was integrated to account for vdW interactions. A non-local correlation energy was incorporated in addition to the semilocal exchange-correlation energy. It was necessary to make adjustments to get accurate contributions from the atom's adjacent spheres, given that vdW density functionals generally yield densities that are less spherical compared to standard GGA functionals. The plane wave basis set was converged using an energy cut-off of 500 eV. A vacuum of 24 Å was applied to minimize the interaction of the heterostructure slab and its periodic images along the z direction. The Brillouin zone was sampled with a  $11 \times 11 \times 1$  k mesh within the Monkhorst-Pack scheme. The convergence criteria of  $10^{-4}$  eV for the total energy and 0.01 eV/Å for force were used for the structural optimization. The formation energy ( $E_f$ ) of the interface between  $M_2CO_2$  and blueP was calculated as follows:

$$E_f = (E_{Total} - (E_{MXene} + E_{blueP})) \quad (1)$$

where,  $E_{Total}$ ,  $E_{MXene}$  and  $E_{blueP}$  represent the energies of the heterostructure, the MXene layer, and blueP layer, respectively.

The charge density difference ( $\Delta\rho$ ) was calculated by,

$$\Delta\rho = \Delta\rho_{MXene/blueP} - \Delta\rho_{MXene} - \Delta\rho_{blueP} \quad (2)$$

where,  $\Delta\rho_{MXene/blueP}$ ,  $\Delta\rho_{MXene}$  and  $\Delta\rho_{blueP}$  represent the total charge density of the MXene/blueP heterostructures, pristine MXene, and blueP monolayers, respectively.

Phonon spectra calculations were carried out using the Phonopy<sup>46</sup> code interfaced with VASP, utilizing harmonic interatomic force constants obtained through density functional perturbation theory (DFPT).<sup>47,48</sup> Supercells of  $4\times 4\times 1$  were employed for these calculations. Thermal stability calculations were conducted at 300 K utilizing *Ab Initio* Molecular Dynamics (AIMD) simulations<sup>49</sup> with the VASP code. Canonical ensemble was employed for molecular dynamics (MD) simulations to achieve atomic structure thermal equilibration. The Noose-Hoover thermostat,<sup>50</sup> as implemented in the VASP package, was utilized within this ensemble including a time step of 1 fs for 3000 steps. Electronic band structures and density of states (DOS) were plotted using the open-source Python package sumo.<sup>51</sup> Visualization of atomic structures and charge density was plotted using the software VESTA.<sup>52</sup>

The thermoelectric properties for all the heterostructures under strain were computed utilizing semi-classical Boltzmann transport theory within the updated Boltztrap2 code,<sup>53</sup> leveraging the electronic structure derived from first-principles calculations. Given that the TE coefficients are significantly dependent on carrier concentration, a rigid band approximation is employed to simulate doping effects. This method presumes that variations in temperature or doping levels do not alter the band structure. We selected a temperature of 900K to focus on high-temperature applications of the material under investigation. A narrower range of charge carrier concentrations was opted for due to the ease of achieving such minimal doping levels in experiments. We have employed the linearized version of the Boltzmann Transport

Equation (BTE) under the Constant Scattering Time Approximation (CSTA), where the transport distribution function is given by;

$$\sigma(\varepsilon, T) = \int \sum_b \mathbf{v}_{b,\mathbf{k}} \otimes \mathbf{v}_{b,\mathbf{k}} \tau_{b,\mathbf{k}} \delta(\varepsilon - \varepsilon_{b,\mathbf{k}}) \frac{d\mathbf{k}}{8\pi^3} \quad (3)$$

where,  $\varepsilon$  is the energy of charge carriers,  $\mathbf{k}$  is the wave vector,  $\mathbf{v}$  is the group velocity of the charge carriers,  $b$  is the index related to energy bands and  $\tau$  is the relaxation time of charge carriers. This is employed to calculate generalized transport coefficient of order  $\alpha$ , as a function of chemical potential  $\mu$  and temperature  $T$  as;

$$\mathcal{L}^{(\alpha)}(\mu; T) = q^2 \int \sigma(\varepsilon, T) (\varepsilon - \mu)^\alpha \left( -\frac{\partial f^{(0)}(\varepsilon; \mu, T)}{\partial \varepsilon} \right) d\varepsilon \quad (4)$$

where  $q$  is the electronic charge, and  $f^{(0)}$  is the Fermi-Dirac distribution function. This further gives the charge and heat currents as;

$$\begin{aligned} j_e &= \mathcal{L}^{(0)} \mathbf{E} + \frac{\mathcal{L}^{(1)}}{qT} (-\nabla T) \\ j_Q &= \frac{\mathcal{L}^{(1)}}{q} \mathbf{E} + \frac{\mathcal{L}^{(2)}}{q^2 T} (-\nabla T) \end{aligned} \quad (5)$$

By considering the two experimental conditions of zero temperature gradient and zero electric current, we can determine the electrical conductivity, Seebeck coefficient, and the electronic contribution to the thermal conductivity as;

$$\begin{aligned} \sigma &= \mathcal{L}^{(0)} \\ S &= \frac{1}{qT} \frac{\mathcal{L}^{(1)}}{\mathcal{L}^{(0)}} \\ \kappa_e &= \frac{1}{q^2 T} \left[ \frac{(\mathcal{L}^{(1)})^2}{\mathcal{L}^{(0)}} - \mathcal{L}^{(2)} \right]. \end{aligned} \quad (6)$$

## 3 RESULTS AND DISCUSSION

### 3.1 Structural and electronic properties of the monolayers

We first optimized the lattice structures of the constituent monolayers of the heterostructures and then calculated their electronic properties. The most stable optimized structures, band structures, and DOS of  $M_2CO_2$  ( $M = \text{Sc}, \text{Hf}, \text{and Zr}$ ) and blueP monolayers are shown in Figure 1. In  $Zr_2CO_2$  and  $Hf_2CO_2$ , the O atoms in the upper (bottom) atomic layer of the MXene structure are positioned directly above (below) the transition metal atoms.<sup>54</sup> Due to this structural and compositional similarity,  $Zr_2CO_2$  and  $Hf_2CO_2$  have many similar properties. On the other hand,  $Sc_2CO_2$  has different sites for the O atoms on the two sides: one functional O layer is positioned at the hollow site of three neighboring C atoms, and the other O atom points to a C atom (Figure 1 (e)), making its configuration asymmetric along the thickness direction. The top view of the blueP structure is similar to the honeycomb lattice of graphene and has two covalently bonded P atoms alternately being displaced out of the 2D plane with an equilibrium distance of 2.26 Å between them.<sup>26</sup> The optimized lattice parameters ( $L_0$ ), band gaps ( $E_g$ ) and work functions ( $\Phi$ ) of the constituent materials of the heterostructure calculated using GGA-PBE functional are given in Table 1, while the bond lengths are presented in Table S1 of the Supporting Information.

Table 1: Lattice parameters ( $L_0$ ), band gaps ( $E_g$ ) and work functions ( $\Phi$ ) of the constituent materials of the heterostructure calculated using GGA-PBE functional

Monolayer	$L_0$ (Å)	$E_g$ (eV)	$\Phi$ (eV)
$Hf_2CO_2$	3.26	0.94	5.29
$Zr_2CO_2$	3.31	0.99	5.18
$Sc_2CO_2$	3.45	1.74	5.35
blueP	3.29	1.99	6.09

The respective band structures and DOS of these monolayers are shown in Figure 1 (b,d,f,h).  $Zr_2CO_2$  and  $Hf_2CO_2$  exhibit similar band dispersion, with indirect band gaps of 0.99 eV and 0.94 eV, respectively. For both materials, the VBM is at the  $\Gamma$  point, and the CBM is at the

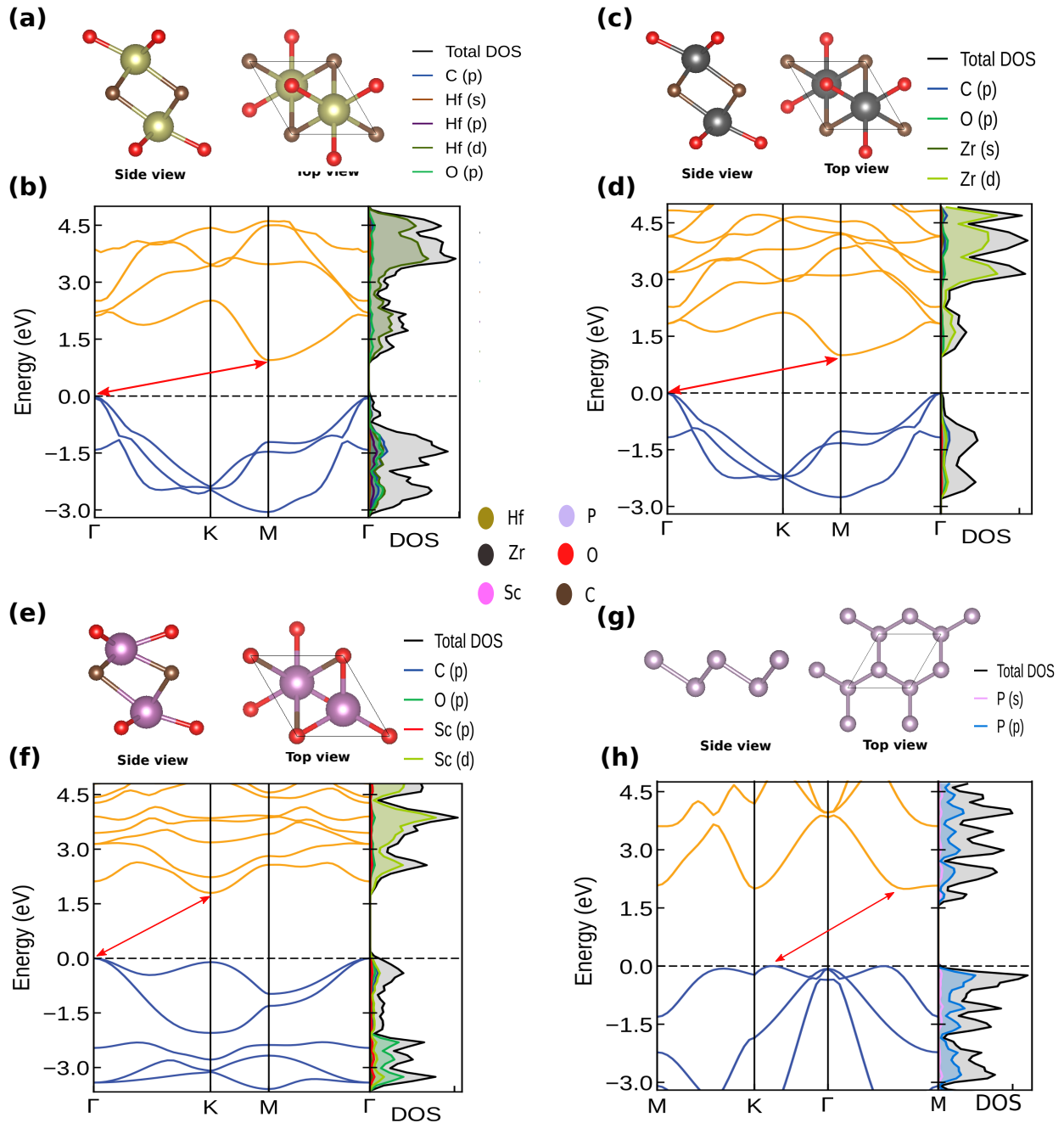


Figure 1: Crystal structure of MXenes  $M_2CO_2$ , (a)  $Hf_2CO_2$ , (c)  $Zr_2CO_2$ , (e)  $Sc_2CO_2$  and (g) blueP and Band structure of MXenes  $M_2CO_2$ , (b)  $Hf_2CO_2$ , (d)  $Zr_2CO_2$ , (f)  $Sc_2CO_2$  and (h) blueP, respectively. The position of the VBM and CBM is illustrated by a double-sided red arrow

M point of the Brillouin zone. The conduction band edge is formed by M-d and O-p states, while the valence band edge is composed of C-p, O-p, and M-d states.  $Sc_2CO_2$  is also an indirect band gap semiconductor, with a band gap of 1.74 eV. However, its band dispersion

differs, with the VBM (CBM) is located at  $\Gamma$  (K) point. The DOS plot reveals that C-p, O-p, and Sc-d states dominate the valence band, while the Sc-d state is dominant in the conduction band. The C-p and Sc-d states are strongly hybridized, which is consistent with the fact that MXenes are mainly assembled through the bond between C and the transition metal atom. The band structure of blueP shows the location of VBM in between K and  $\Gamma$  point and CBM in between  $\Gamma$  and M point giving an indirect band gap of 1.99 eV. Both the valence and conduction bands are predominantly derived from P-p states.

### 3.2 MXenes ( $M_2CO_2$ ) and blueP heterostructures

The lattice mismatches between  $M_2CO_2$  (M= Hf, Zr, Sc) and blueP are 0.91%, 0.60% and 4.6%, respectively, which all are within the acceptable range of 5% and their interface is flexible enough to accommodate this lattice mismatch, indicating that these heterostructures can be synthesized experimentally.<sup>55</sup> We have considered 6 different stackings of MXene/blueP heterostructures to determine the most stable configuration. These configurations are all properly optimized. Figure S1 and Figure S2 in the Supporting Information illustrate the stacking configurations considered for the (M = Hf, Zr) $_2CO_2$ /blueP and Sc $_2CO_2$ /blueP vdW heterostructures, respectively. To verify the thermodynamic stability of the most favorable stacking within this set of configurations, we have computed the formation energy. The calculated formation energies for different stackings are listed in Table S2 in the Supporting Information. It is noteworthy that all configurations exhibit negative formation energies, signifying the energetically viable nature of  $M_2CO_2$ /blueP heterostructure fabrication. In accordance with the fundamental principle that a more negative formation energy indicates greater stability, we have considered the most stable structure for our further study, as indicated in bold in Table S2 in the Supporting Information. The optimized interlayer distance for these most stable stackings are found to be 2.94Å, 2.89Å and 2.50Å for Hf $_2CO_2$ /blueP, Zr $_2CO_2$ /blueP and Sc $_2CO_2$ /blueP, respectively. These values match well with the previous reports for these heterostructures.<sup>31,32</sup>

The atomic structure, band structure, and DOS of  $M_2CO_2$  (M=Hf, Zr, Sc)/blueP heterostructures are shown in Figure 2. The results reveal that  $Hf_2CO_2/blueP$ ,  $Zr_2CO_2/blueP$ , and  $Sc_2CO_2/blueP$  all exhibit indirect band gaps, with values of 1.04 eV, 0.95 eV, and 1.06 eV, respectively. In each case, the VBM is located at the  $\Gamma$  point, while the CBM is at the M point. The projected band structures indicate that in both  $Hf_2CO_2/blueP$  and  $Zr_2CO_2/blueP$ , the CBM and VBM are predominantly influenced by the MXene layer. Specifically, the VBM is primarily determined by C-p and O-p states, while the CBM is influenced by the d states of Hf (or Zr) atoms, classifying these as type-I heterostructures. There is a small reduction of band gap in  $Sc_2CO_2/blueP$  as compared to pristine layers suggesting significant inter-layer interactions and charge redistribution in this heterostructure. BlueP has more contribution in the CBM (P-p states), while the VBM (Sc-d and O-p states) is mainly contributed from  $Sc_2CO_2$  monolayer, indicating a type-II band alignment.

To verify the dynamic stability of the heterostructures, we performed phonon spectrum calculations, as depicted in Figure 3 (a-c). The absence of imaginary frequencies in the phonon spectra confirms the dynamical stability of the MXene/blueP heterostructures. Although there is a small U-shaped feature near the  $\Gamma$  point in the phonon spectra, it does not indicate lattice instability. Instead, this feature represents the flexural acoustic mode characteristic of 2D systems.<sup>56</sup> To further assess the thermal stability of the  $M_2CO_2/blueP$  heterostructures, we conducted *ab initio* molecular dynamics (AIMD) simulations using the Nose-Hoover heat bath scheme.<sup>57</sup> The simulations were performed on a  $3 \times 3 \times 1$  supercell over a period of 3000 fs at 300 K. The temperature evolution throughout the simulation is shown in Figure 3 (d-f). The observed convergence of temperature at the end of the simulation steps, affirms the robustness and accuracy of the obtained results. These results affirm the thermal stability of the considered heterostructures at room temperature (300 K), rendering them viable candidates for future nanoelectronic applications.

In addition, the mechanical stability of all considered monolayers and heterostructures has

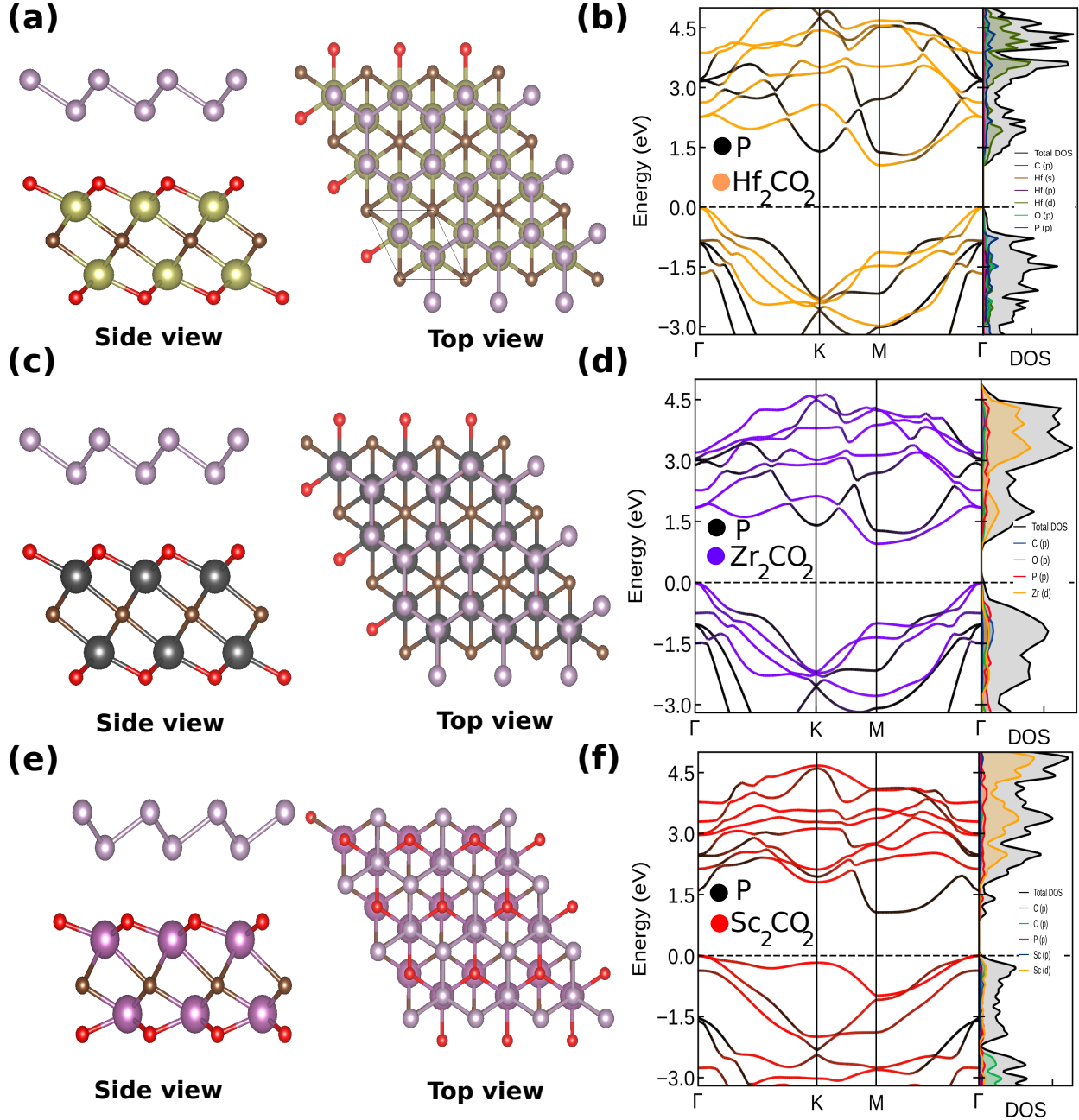


Figure 2: Crystal structure of MXene/blueP heterostructures (a)  $\text{Hf}_2\text{CO}_2/\text{blueP}$ , (c)  $\text{Zr}_2\text{CO}_2/\text{blueP}$ , and (e)  $\text{Sc}_2\text{CO}_2/\text{blueP}$  and Band structure of (b)  $\text{Hf}_2\text{CO}_2/\text{blueP}$ , (d)  $\text{Zr}_2\text{CO}_2/\text{blueP}$ , and (f)  $\text{Sc}_2\text{CO}_2/\text{blueP}$ , respectively

been verified. The elastic constants were calculated to evaluate the mechanical stability of blueP,  $\text{Hf}_2\text{CO}_2$ ,  $\text{Zr}_2\text{CO}_2$ ,  $\text{Sc}_2\text{CO}_2$ , and their corresponding heterostructures ( $\text{Hf}_2\text{CO}_2/\text{blueP}$ ,  $\text{Zr}_2\text{CO}_2/\text{blueP}$ , and  $\text{Sc}_2\text{CO}_2/\text{blueP}$ ). Since these materials exhibit an isotropic hexagonal lattice, the elastic tensor components are reduced to three key constants:  $C_{11}$ ,  $C_{12}$ , and  $C_{66}$

(with  $C_{66} = (C_{11} - C_{12})/2$ ), where  $C_{ij}$  represents the second-order elastic constant, in unit of N/m, for two-dimensional materials.<sup>58</sup> Only two independent elastic constants,  $C_{11}$  and  $C_{12}$ , are required to describe the system. These constants were obtained through the stress-strain relationship by applying a minor strain to the equilibrium lattice configuration. The values of  $C_{11}$ ,  $C_{12}$ ,  $C_{66}$  meet the mechanical stability criteria ( $C_{11} > 0$  and  $C_{11} > |C_{12}|$ ), as shown in supplementary Figure S3, confirming the mechanical stability of both the monolayers and heterostructures.

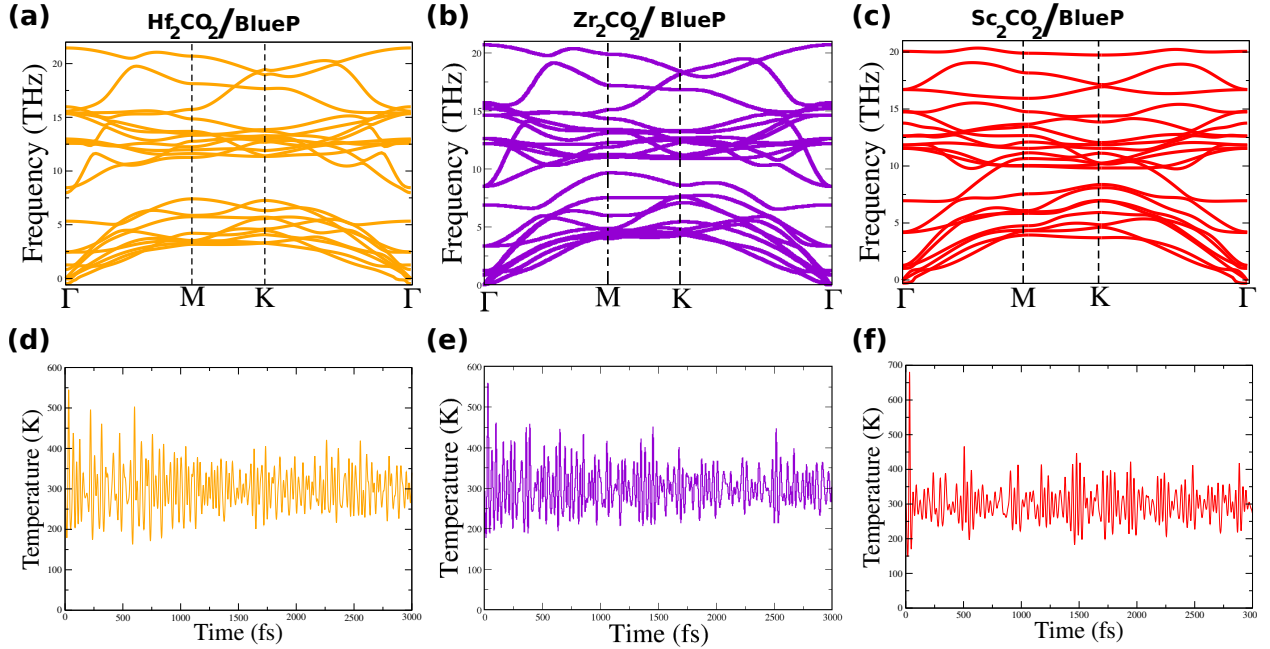


Figure 3: Phonon band structure of heterostructures, (a)  $\text{Hf}_2\text{CO}_2/\text{blueP}$ , (b)  $\text{Zr}_2\text{CO}_2/\text{blueP}$ , and (c)  $\text{Sc}_2\text{CO}_2/\text{blueP}$  and Thermal stability at 300 K of heterostructures (d)  $\text{Hf}_2\text{CO}_2/\text{blueP}$ , (e)  $\text{Zr}_2\text{CO}_2/\text{blueP}$ , and (f)  $\text{Sc}_2\text{CO}_2/\text{blueP}$ , respectively

The work function is a key parameter that describes a material's ability to release electrons from its surface. It is defined as the energy required for an electron to transition from the Fermi level to the vacuum level. The work function ( $\Phi$ ) can be calculated as the difference between the vacuum ( $E_{vac}$ ) and the Fermi level ( $E_F$ ). Mathematically, it is expressed as;

$$\Phi = E_{vac} - E_F \quad (7)$$

The energy level  $E_{vac}$  is identified in the electrostatic potentials along the z-direction, as

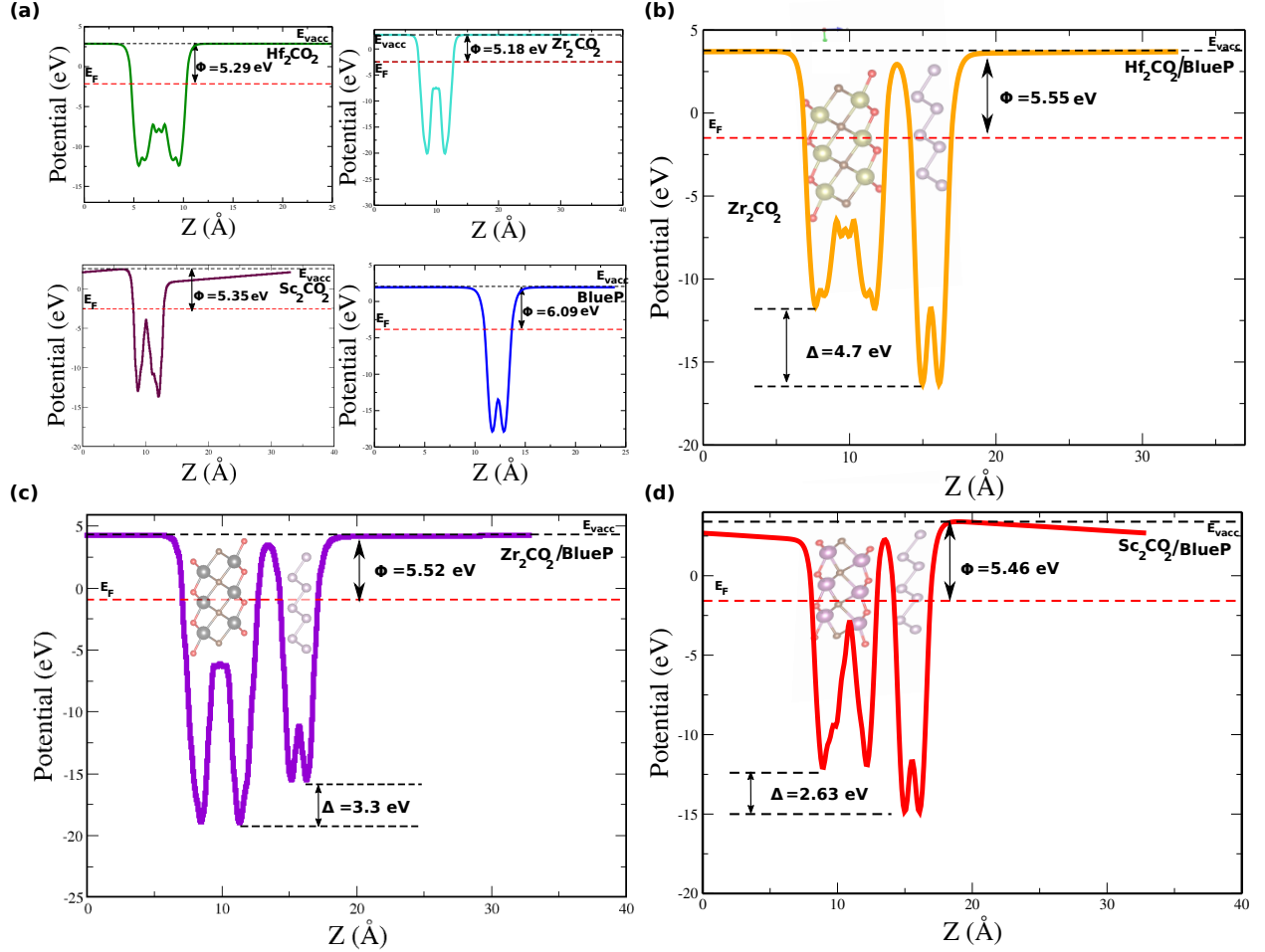


Figure 4: (a) Electrostatic Potential of monolayers and Electrostatic Potential of heterostructures (b)  $\text{Hf}_2\text{CO}_2/\text{blueP}$ , (c)  $\text{Zr}_2\text{CO}_2/\text{blueP}$ , and (d)  $\text{Sc}_2\text{CO}_2/\text{blueP}$ , respectively. The black dotted line represents  $E_{vac}$ , while the red dotted line indicates  $E_{Fermi}$

shown in Figure 4 by the black dotted line. The  $E_F$  level is obtained from first-principles calculations, indicated by the red dotted line. For  $\text{Sc}_2\text{CO}_2$ , its asymmetric atomic structure<sup>9</sup> induces a spontaneous polarization that results in an internal electric field between the two sides of the monolayer.<sup>59</sup> As a result, the electrostatic potential shows an asymmetry in the vacuum levels for two surfaces of the  $\text{Sc}_2\text{CO}_2$  monolayer. The work function values of the monolayers are tabulated in Table 1. Electrons preferentially move from lower to higher work function materials, seeking a lower energy state while forming heterostructures. The result indicated that when the monolayer MXene interacted with the monolayer blueP to form the

MXene/blueP heterostructure the electrons would flow from the MXene to blueP, regardless of the band alignment and CBM position, until they reached the same Fermi levels. This transfer results in Fermi level adjustments with respect to the vacuum level: an elevation in blueP and a corresponding reduction in MXene, establishing work function values of 5.55, 5.52, and 5.46 for  $\text{Hf}_2\text{CO}_2/\text{blueP}$ ,  $\text{Zr}_2\text{CO}_2/\text{blueP}$ , and  $\text{Sc}_2\text{CO}_2/\text{blueP}$ , respectively.

The electrostatic potential energy graph of the heterostructures is shown in Figure 4 (b-d). The potential drops across the interfaces are 4.7, 3.3, and 2.63 eV for the  $\text{Hf}_2\text{CO}_2/\text{blueP}$ ,  $\text{Zr}_2\text{CO}_2/\text{blueP}$ , and  $\text{Sc}_2\text{CO}_2/\text{blueP}$  heterostructures, respectively. These values indicate the presence of a strong electrostatic field perpendicular to the interface. In type-II heterostructures, this built-in electric field is crucial for controlling the recombination of electron-hole pairs and significantly enhancing the migration of photogenerated charges. Effective separation of these charge carriers is essential for maximizing efficiency in photovoltaic applications, as electron-hole pairs generated by incident photons often recombine within the semiconductor or at the surface before contributing to photocatalytic effects. Type-II band alignment is particularly advantageous, as it facilitates the separation of charge carriers by allowing electrons to migrate to the CBM of one layer while holes remain confined to the VBM of the other layer.<sup>33</sup> The built-in electric field in these heterostructures effectively separates the electron-hole pair and reduces charge recombination, significantly boosting the photocatalytic performance of the materials. This improvement in charge separation and transport markedly boosts the photocatalytic performance of these materials. Additionally, the enhanced sensitivity provided by the built-in electric field is effective in detecting minor changes in environmental conditions, making these heterostructures valuable for sensor applications.

The formation of a heterostructure induces interactions between the layers, resulting in charge transfer and redistribution at the interface. This phenomenon is examined by calculating the charge density difference of the heterostructure, as shown in Figure 5 (a-c). The charge density difference plots are derived by subtracting the charge densities of the individ-

ual layers in the unit cell from that of the heterostructure. For a more detailed analysis of the charge transfer processes, the planar charge density difference along the z-direction was also calculated, as depicted in Figure 5 (d-f). In the  $\text{Hf}_2\text{CO}_2/\text{blueP}$  and  $\text{Zr}_2\text{CO}_2/\text{blueP}$  heterostructures, charge redistribution is primarily localized around the interface. Since there is no complete charge carrier separation, these two combinations would not be beneficial for photocatalytic applications. In contrast, the  $\text{Sc}_2\text{CO}_2/\text{blueP}$  heterostructure exhibits charge accumulation in the blueP layer, indicating effective charge carrier separation and enhancing its photocatalytic efficiency. Further charge analysis using the Bader method provides quantitative results regarding charge transfer in the MXene/blueP heterostructures, as summarized in Table S3 in the Supporting Information. From the computed Bader charges, we found that the amount of charge transfer correlates with the interlayer interaction across the interface. Our results show that the charge transfer per unit cell is about 0.0144  $|e|$  in  $\text{Hf}_2\text{CO}_2/\text{blueP}$ , 0.0149  $|e|$  in  $\text{Zr}_2\text{CO}_2/\text{blueP}$ , and 0.0135  $|e|$  in  $\text{Sc}_2\text{CO}_2/\text{blueP}$  heterostructures.

### 3.3 Application of external strain on $\text{M}_2(\text{M}=\text{Hf, Zr, Sc})\text{CO}_2/\text{blueP}$ heterostructure

Nanoelectronics and optoelectronics greatly benefit from materials whose electronic properties, particularly the band gap, can be adjusted by external factors such as strain, electric field, and interlayer distance.<sup>60</sup> The physical properties of 2D layered materials are known to be highly sensitive to external influences. In experimental fabrication processes involving 2D materials on a substrate, mismatches between the 2D material and the substrate can lead to crystal distortion, inducing strain or stress effects. Consequently, a comprehensive understanding of the electronic properties of these heterostructures is crucial for optimizing their performance in future applications.

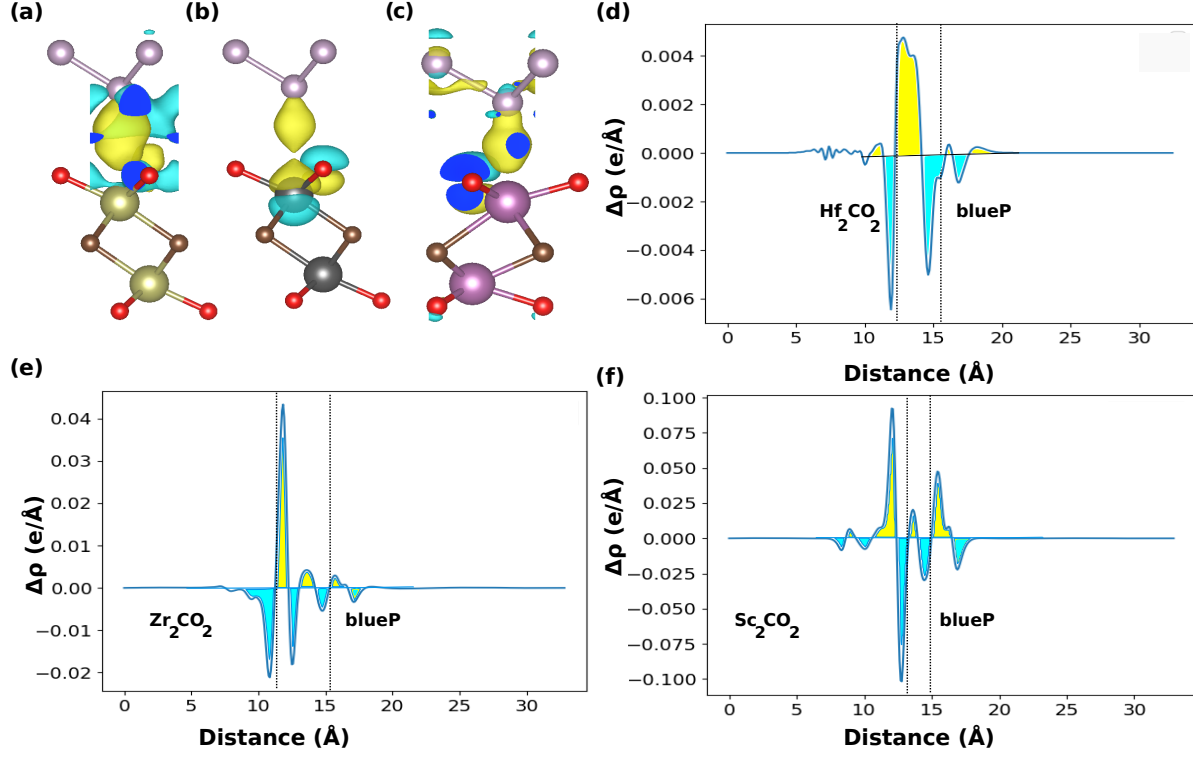


Figure 5: Charge density difference plot of heterostructures, (a)  $\text{Hf}_2\text{CO}_2/\text{blueP}$ , (b)  $\text{Zr}_2\text{CO}_2/\text{blueP}$ , and (c)  $\text{Sc}_2\text{CO}_2/\text{blueP}$  and Planar charge density of heterostructures (d)  $\text{Hf}_2\text{CO}_2/\text{blueP}$ , (e)  $\text{Zr}_2\text{CO}_2/\text{blueP}$ , and (f)  $\text{Sc}_2\text{CO}_2/\text{blueP}$  respectively. Yellow and cyan represent charge accumulation and charge depletion, respectively and the area between the dashed lines represents the interface of MXene/blueP heterostructure

**Biaxial strain** : First, we applied biaxial strain on the three heterostructures by changing its in-plane lattice parameters along the a and b axis equally. The applied strain was calculated as,  $\epsilon = (L - L_0)/L_0$ , where L and  $L_0$  represent the lattice parameter of the strained and the unstrained structure, respectively. The band gap of the three MXene/blueP heterostructures changes as a function of the biaxial strain, shown in Figure 6(a). The response of  $\text{Zr}_2\text{CO}_2/\text{blueP}$  and  $\text{Hf}_2\text{CO}_2/\text{blueP}$  to varying strain percentages exhibit remarkable similarities: a discernible reduction in the band gap for both compressive and tensile strain. Both the heterostructures undergo a transition to a metallic state at a compressive strain of 7%. An increase and decrease in band gap were observed after a tensile strain value of 8% (9%) in  $\text{Zr}_2\text{CO}_2/\text{blueP}$  ( $\text{Hf}_2\text{CO}_2/\text{blueP}$ ), where the band gap attains the first minima.  $\text{Zr}_2\text{CO}_2/\text{BlueP}$  and  $\text{Hf}_2\text{CO}_2/\text{blueP}$  undergo metallic transition at tensile strains of 18% and

14%, respectively. In contrast, the  $\text{Sc}_2\text{CO}_2/\text{blueP}$  heterostructure demonstrates a distinctive behavior in its band gap response. Initially, the band gap demonstrates an upward trend under compressive strain, then starts decreasing, and ultimately, it transforms into a metallic state at a compressive strain of 10%. Under tensile strain, the band gap exhibits a sharp decrease, and the material transitions to a metallic state at a strain of 7%.

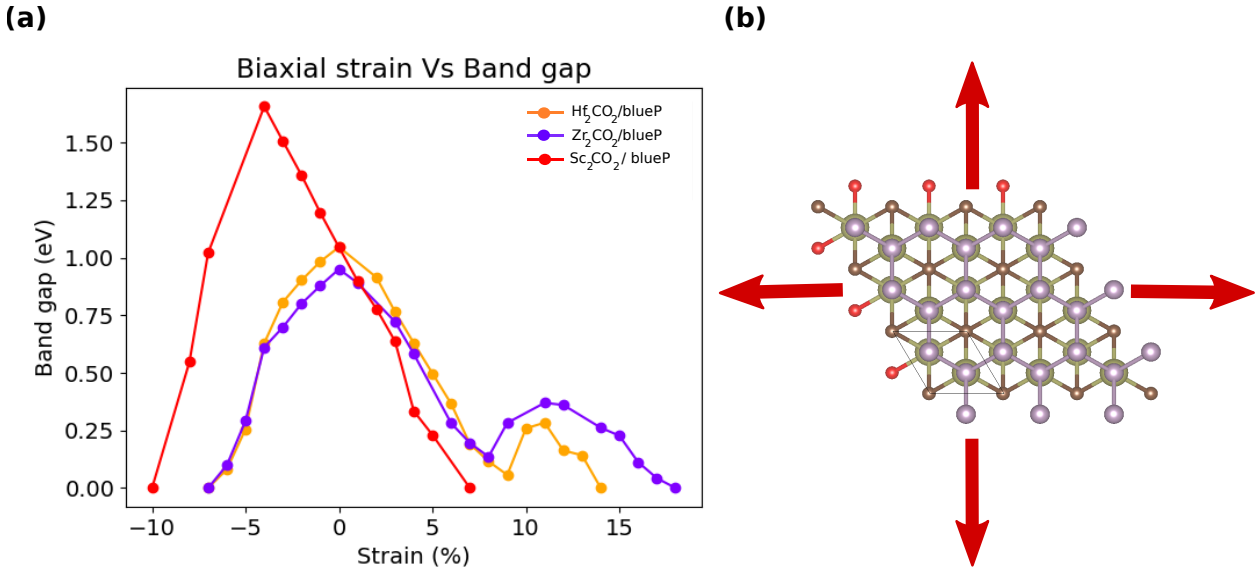


Figure 6: (a) The change in bandgaps of MXene/blueP heterostructures under various percentages of applied biaxial strain and (b) Schematic of biaxial strain

By examining the band structure and partial density of states (PDOS) of the  $\text{M}_2\text{CO}_2/\text{blueP}$  heterostructure under both compressive and tensile strain, we gained deeper insights into how biaxial strain affects its electronic structure. Figure 7 shows the bandstructure and PDOS plot of  $\text{Hf}_2\text{CO}_2/\text{blueP}$  under different percentages of biaxial strain. For an unstrained heterostructure of  $\text{Hf}_2\text{CO}_2/\text{blueP}$ , the conduction band is predominantly influenced by the Hf-d state, and the valence band is dominated by C-p and O-p states. The VBM is located at the  $\Gamma$  point and the CBM at the M point. As we increase the compressive strain, the CBM at the M point decreases and the VBM at the  $\Gamma$  point increases, crossing the fermi level at -7%, resulting in a metallic transition. In the case of tensile strain, the band gap is reduced till 9%, where CBM decreases at M point with strain. At 10%, the CBM shifts slightly upward, causing the band gap to increase slightly. With further increase in strain, the CBM shifts

from the M point to the  $\Gamma$  point at 12% strain, and the VBM also shifts away from the  $\Gamma$  point. A semiconductor-to-metal transition (S-M transition) occurs when the CBM crosses the Fermi level at 14% strain. Under increasing compressive strain, the contribution of the P-p orbitals to the valence band increases, while the conduction band remains dominated by the C-p and O-p orbitals (see Figure 7 (b)), leading to a transition from type-I to type-II. To gain visual insight, we performed band-decomposed charge density calculations as depicted in Figure 7 (g). Our analysis revealed that CBM and VBM contributions of  $\text{Hf}_2\text{CO}_2/\text{blueP}$  originate from the  $\text{Hf}_2\text{CO}_2$  layer without any strain application. Notably, upon reaching a 2 % strain, a type-II transition becomes evident, with the blueP layer’s contribution to the CBM becoming distinctly observable. At -5% strain, the VBM is predominantly contributed by the P-p states, while the CBM is primarily influenced by the Hf-d and O-p states. This finding strongly supports the transition from type-I to type-II behavior, as is also evident from the band-decomposed charge density plot. The changes in bandstructure and partial density of states of  $\text{Zr}_2\text{CO}_2/\text{blueP}$  under different biaxial strains are given in the Supporting Information Figure S4.  $\text{Zr}_2\text{CO}_2/\text{blueP}$  heterostructure also shows a similar pattern of band gap change while applying biaxial strain.

The  $\text{Sc}_2\text{CO}_2/\text{blueP}$  heterostructure exhibits a different trend in band dispersion compared to the  $\text{Hf}_2\text{CO}_2/\text{blueP}$  and  $\text{Zr}_2\text{CO}_2/\text{blueP}$  heterostructures under biaxial strain, as shown in Figure 8. From the band edge position under compressive strain, the position of CBM initially rises at the M point, reaching a maximum band gap of 1.7 eV at -4% strain. Beyond this point, the CBM shifts from M to K and begins to decrease, crossing the Fermi level at -9% strain. Concurrently, the VBM also moves towards the Fermi level with increasing strain. Under tensile strain, both the CBM and VBM shift towards the Fermi level as the strain increases. Initially, the VBM is at the  $\Gamma$  point, but at 3% strain, it shifts to the K point and crosses the Fermi level, resulting in an S-M transition at 6%. For better comparison, we have plotted the changes in the VBM and CBM under different biaxial strains, as shown in Figure S5 in the Supporting Information. The analysis of the partial density of states re-

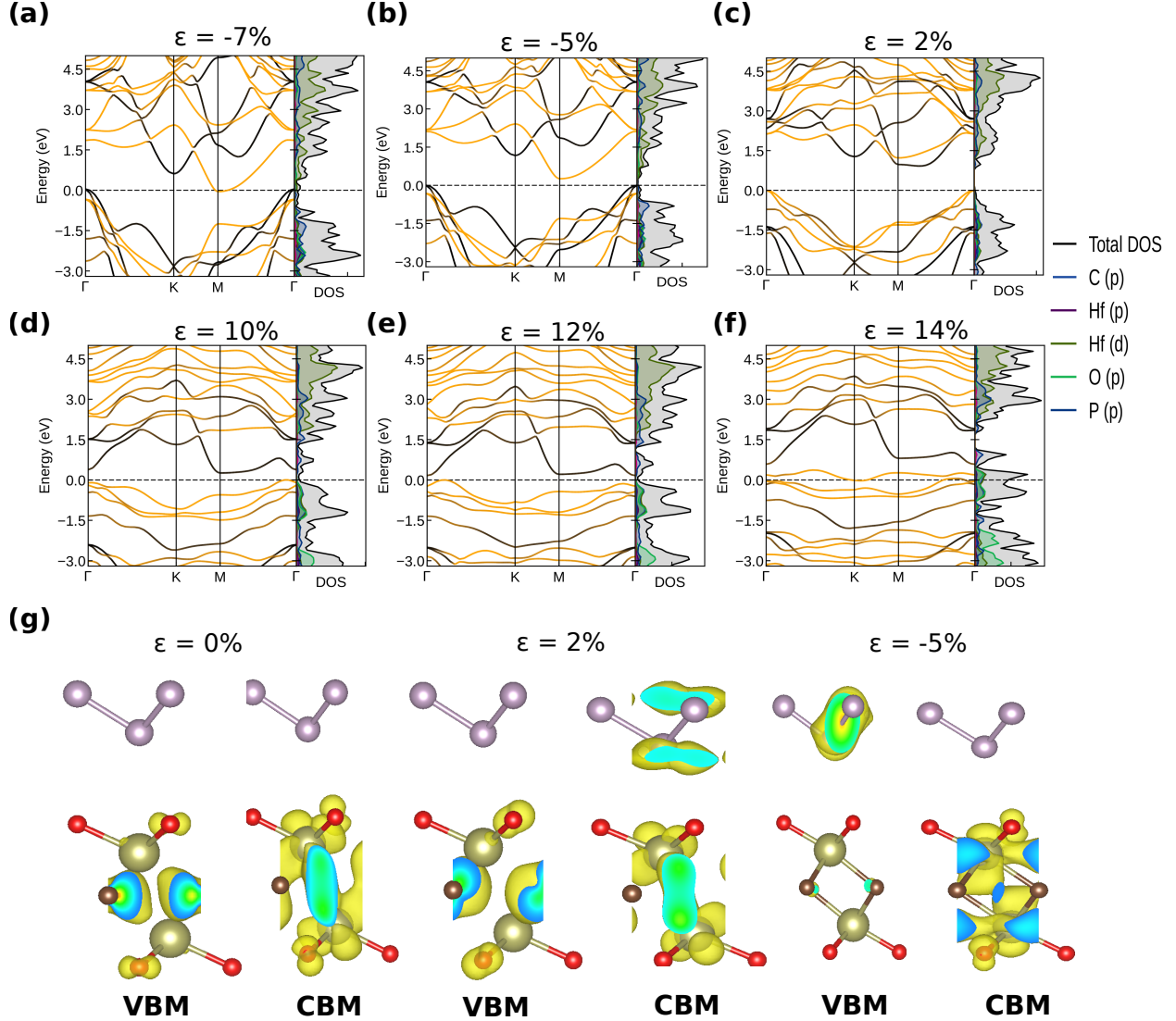


Figure 7: Band structures, PDOS [(a)-(f)] and (g) Band decomposed charge density of  $\text{Hf}_2\text{CO}_2/\text{blueP}$  heterostructures under different percentages of biaxial strain

veals significant insights into the behavior of the conduction and valence bands under strain. Throughout the application of tensile strain, we consistently observe the contribution of the p state of blueP to the CBM, while the VBM is primarily influenced by the Sc-d along with the O-p states. However, under compressive strain, a noticeable shift occurs. Up to -4% strain, the VBM is primarily contributed to by the Sc-d and the C-p states, while the CBM is influenced by the P-p states. Beyond -4%, a gradual change is observed: the contribution of p state of blueP in the VBM and the Sc-d states in the CBM becomes more pronounced. At

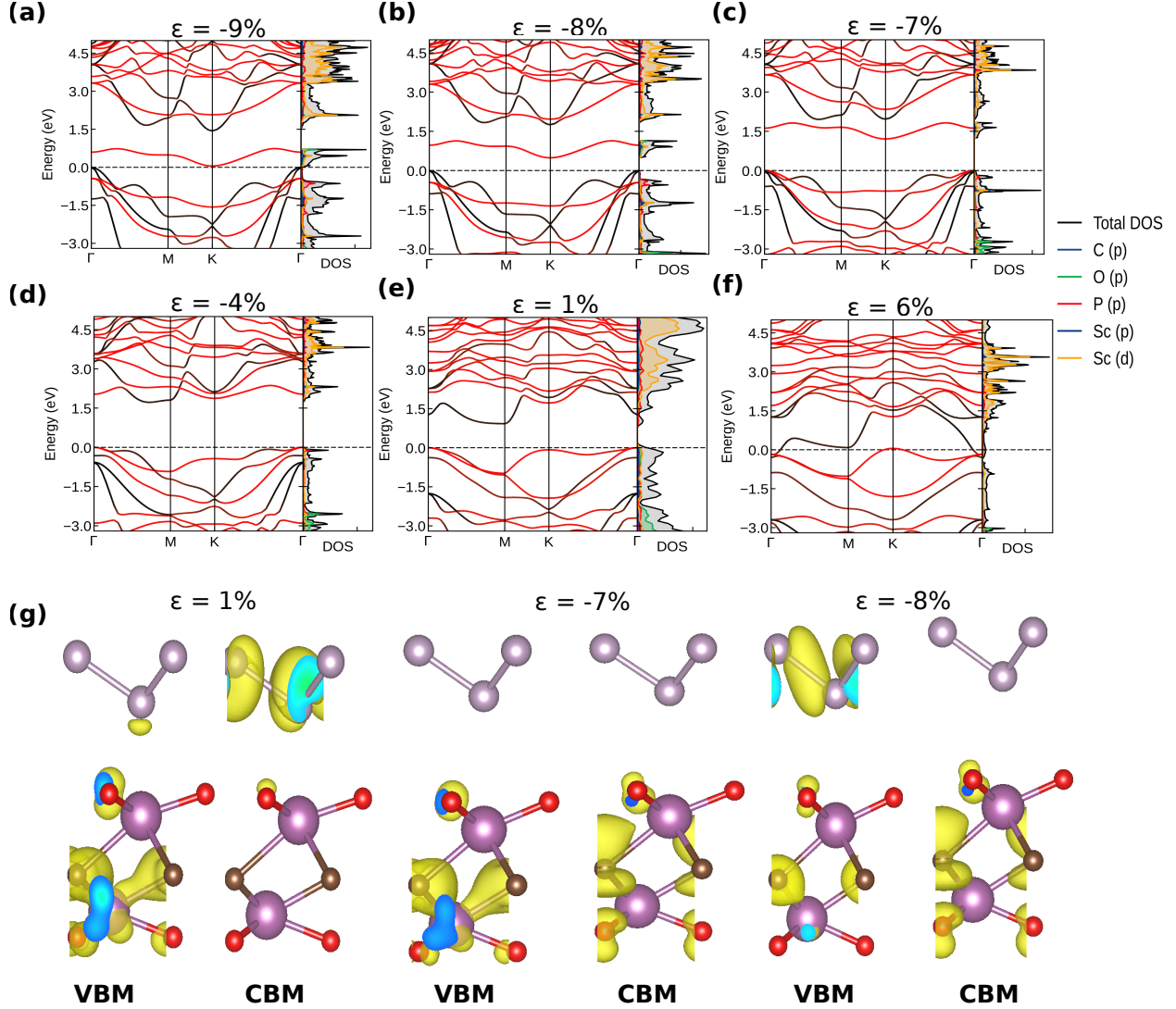


Figure 8: Band structures, PDOS [(a)-(f)] and (g) Band decomposed charge density of  $\text{Sc}_2\text{CO}_2/\text{blueP}$  heterostructures under different percentages of biaxial strain

-5% strain, the VBM is entirely dominated by the p states of blueP, and the CBM is mainly influenced by Sc-d states. A notable transition from type-II to type-I behavior is observed at -7% strain, where both the VBM and CBM are dominated by Sc-d states. However, at -8% strain, the behavior reverts to type-II, with the VBM again dominated by P-p state and the CBM influenced by Sc-d states.

Uniaxial strain along zig-zag and armchair direction : It has been already observed

from the previous section that strain shows remarkable effects in modifying the electronic properties of  $M_2CO_2$ /blueP heterostructure. In this section, we will examine the effects of uniaxial strain applied along both the zigzag and armchair directions (see schematic Figure 9(c)) on the electronic properties of the three  $M_2CO_2$ /blueP heterostructures. Applying strain along these directions provides a powerful means to tailor material properties, optimize device performance, and develop advanced technologies across various fields, including electronics and photonics. This approach enables the design of materials with specific characteristics to meet diverse application requirements.<sup>61</sup>

We found that the changes in the band gap for  $Hf_2CO_2$ /blueP and  $Zr_2CO_2$ /blueP under uniaxial strain along both the zigzag and armchair directions show similar trends (see Figure 9). When strain is applied along the zigzag direction, the band gap decreases for both tensile and compressive strain, with metallic transitions occurring when strain exceeds certain critical values. Although a similar S-M transition was observed for compressive strain along the armchair direction, no metallic transition was observed under tensile strain. Instead, the band gap reduces for the initial values of strain, but for larger values, there is a small increment in the band gap, which starts to decrease again reaching a minimal value of 0.016 eV for  $Zr_2CO_2$ /blueP at +19% strain. Similarly, for  $Hf_2CO_2$ /blueP, the band gap reaches a minimal value of 0.003 eV at 18% strain. The band gap opens up again for larger strain for both the heterostructures.  $Sc_2CO_2$ /blueP shows a different behavior in a change in band gap under uniaxial strain than that of the other two heterostructures. For strain along armchair direction, the band gap was found to be decreasing and becoming metallic for tensile strain of 10 %. Whereas for compressive strain, the band gap is found to be increasing first, then becomes constant for initial values of strain and after 4%, the band gap started reducing and became metallic for 16% compressive strain. A similar trend was observed for strain along zig-zag directions too.

To observe the changes in band dispersions under uniaxial strain, we have plotted the band

structures, PDOS, and band-decomposed charge density for  $\text{Zr}_2\text{CO}_2/\text{blueP}$  in the zigzag and armchair directions, as shown in Figures 10 and 11, respectively. For strain applied in the zigzag direction, the CBM shifts closer to the Fermi level and crosses it, leading to a metallic transition for both compressive and tensile strain at the K point. From the band structure, it is visible that there is a transition from type-I to type-II for 7% of compressive strain and 4% of tensile strain. The band decomposed charge density plot for the  $\text{Zr}_2\text{CO}_2/\text{blueP}$  heterostructure under zigzag strain, as depicted in Figure 10 (g), offers valuable insights. Initially, at zero strain, both the VBM and CBM are primarily attributed to the  $\text{Zr}_2\text{CO}_2$  layer, indicating a type-I heterostructure configuration. However, as the zigzag strain is applied, a transition to a type-II heterostructure becomes evident in both plots. The analysis of the partial density of states further elucidates the strain-dependent behavior. Up to 3% tensile strain, the VBM is chiefly influenced by the Zr-d states, along with contributions from the O-p and C-p states, while the CBM is predominantly governed by the Zr-d states. Beyond 3%, the CBM increasingly reflects the influence of the p state of blueP while maintaining VBM dominance by the Zr-d states, where the type-I to type-II transition occurs. In the case of compressive strain, the CBM is primarily contributed to by the Zr-d states, while the VBM sees significant contributions from the C-p, Zr-d, and O-p states. Notably, at -7% strain, there's a marked increase in the involvement of the p state of blueP to the VBM, accompanied by a type-II transition.

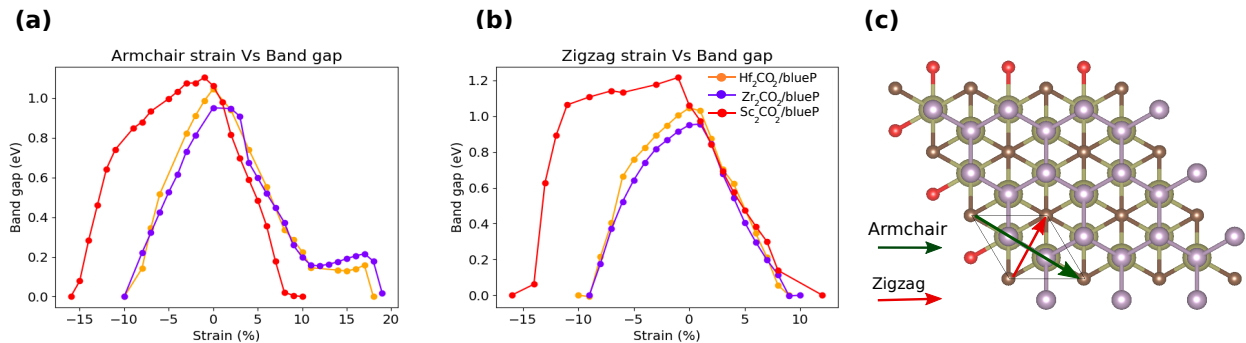


Figure 9: The change in bandgaps of MXene/blueP heterostructures under various percentages of applied uniaxial strain (a) armchair (b) zigzag, and (c) the schematic of uniaxial strain along the zigzag and armchair directions

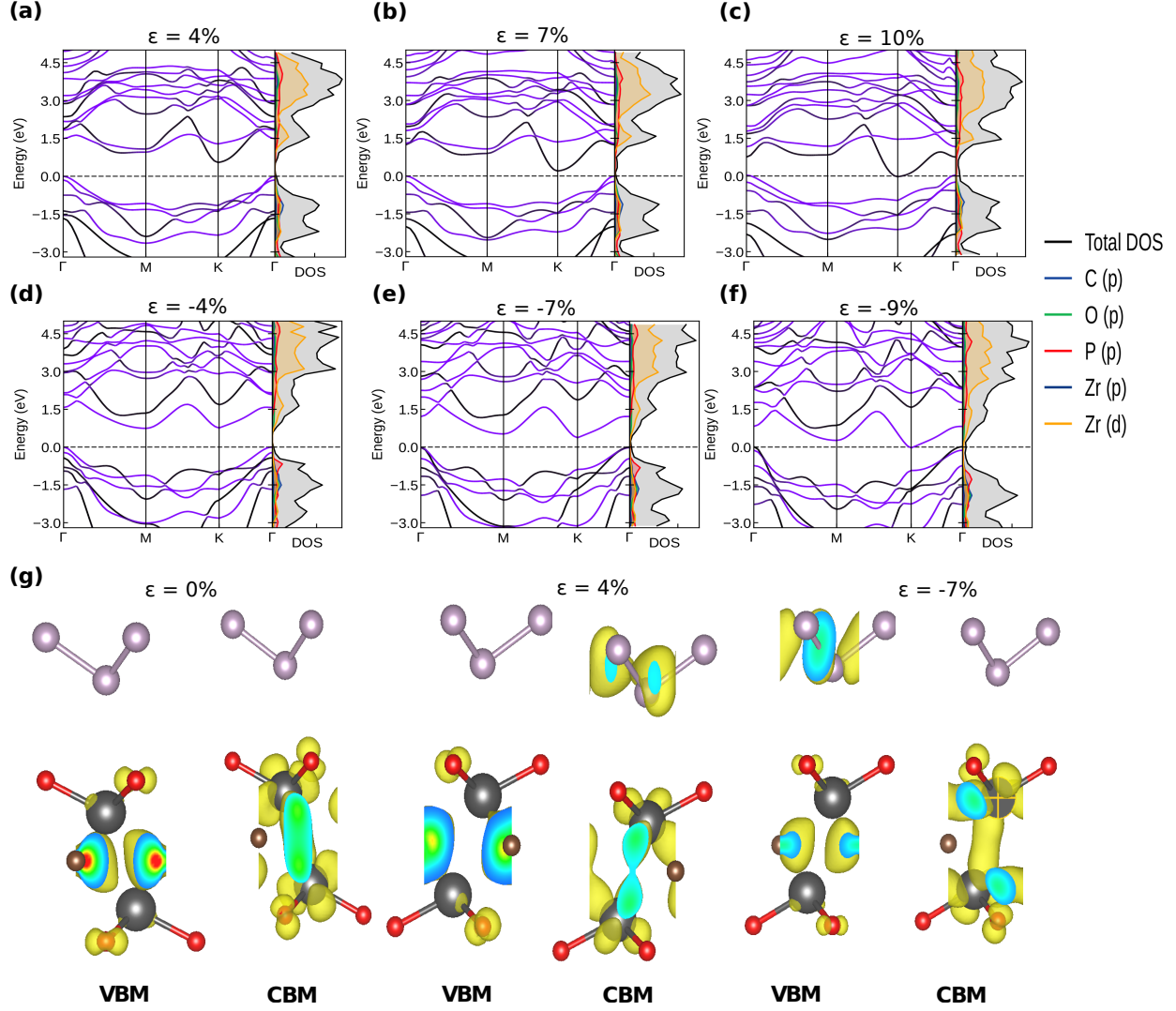


Figure 10: Band structures, PDOS [(a)-(f)] and (g) Band decomposed charge density of  $\text{Zr}_2\text{CO}_2/\text{blueP}$  heterostructures under different percentages of uniaxial strain along zigzag direction

The band structures for strain along the armchair direction are plotted in Figure 11. There is a transition from type-I to type-II occurs for tensile strain as well as compressive strain. The CBM shifts towards the Fermi level at the M point with an increase in both compressive and tensile strain, leading to a reduction in the band gap. The metallic transition happens when CBM (VBM) crosses the Fermi level at M ( $\Gamma$ ) point under compressive strain of 10%. A shift in VBM position from  $\Gamma$  point was observed when the tensile strain value was higher than 13%. No metallic transition was observed within the tensile strain range applied here. The

band-decomposed charge density for  $\text{Zr}_2\text{CO}_2/\text{blueP}$ , illustrated in Figure 11(g), indicates a type-II heterostructure under strain in the armchair direction. The PDOS analysis reveals significant findings regarding the behavior under armchair strain. Initially, at the onset of tensile strain, the VBM is primarily influenced by the C-p states and Zr-d state, while the CBM is largely contributed to by the Zr-d state. However, at 6% strain, there's a notable increase in the contribution of the p state of blueP to the CBM, and type-II transition occurs. Conversely, under compressive strain, at 9%, there is a marked increase in the involvement of the p states of blueP in the VBM, also leading to a type-II transition

The change in the band structure of  $\text{Hf}_2\text{CO}_2/\text{blueP}$  under different percentages of strain in the zigzag and armchair directions is displayed in the Supporting Information (Figures S5 and S6). Applying 2% tensile strain and 7% compressive strain in the armchair direction induces a transition from type-I to type-II. For strain applied in the zigzag direction, the transition from type-I to type-II occurs at 1% tensile strain and 6% compressive strain. For the armchair direction, a S-M transition is observed only with compressive strain (10%). The bandgap nearly closes at 18% tensile strain but starts to reopen at higher strains. Conversely, in the zigzag direction, the S-M transition occurs at 9% tensile strain and 10% compressive strain. The band decomposed charge density plot for different strain percentages along zigzag and armchair is shown in the Supporting Information Figure S6 and Figure S7 (g).

Figure 12 shows the change in the band structure of the  $\text{Sc}_2\text{CO}_2/\text{blueP}$  heterostructure under different percentage of uniaxial strain in the armchair direction. For tensile strain, we found that at 6% of strain, there is a transition from indirect to direct band gap, and for the 10% the band gap closes when the CBM crosses the Fermi level at the  $\Gamma$  point. In the case of compressive strain, the band is found to be constant for initial values of strain, and after -5% the conduction band started decreasing. CBM is mainly contributed by the p state of blueP and VBM is by Sc-d state. At -13 % the contribution of p state of blueP has slightly increased in the VBM, but there is no type-II to type-I transition occurring. Then finally

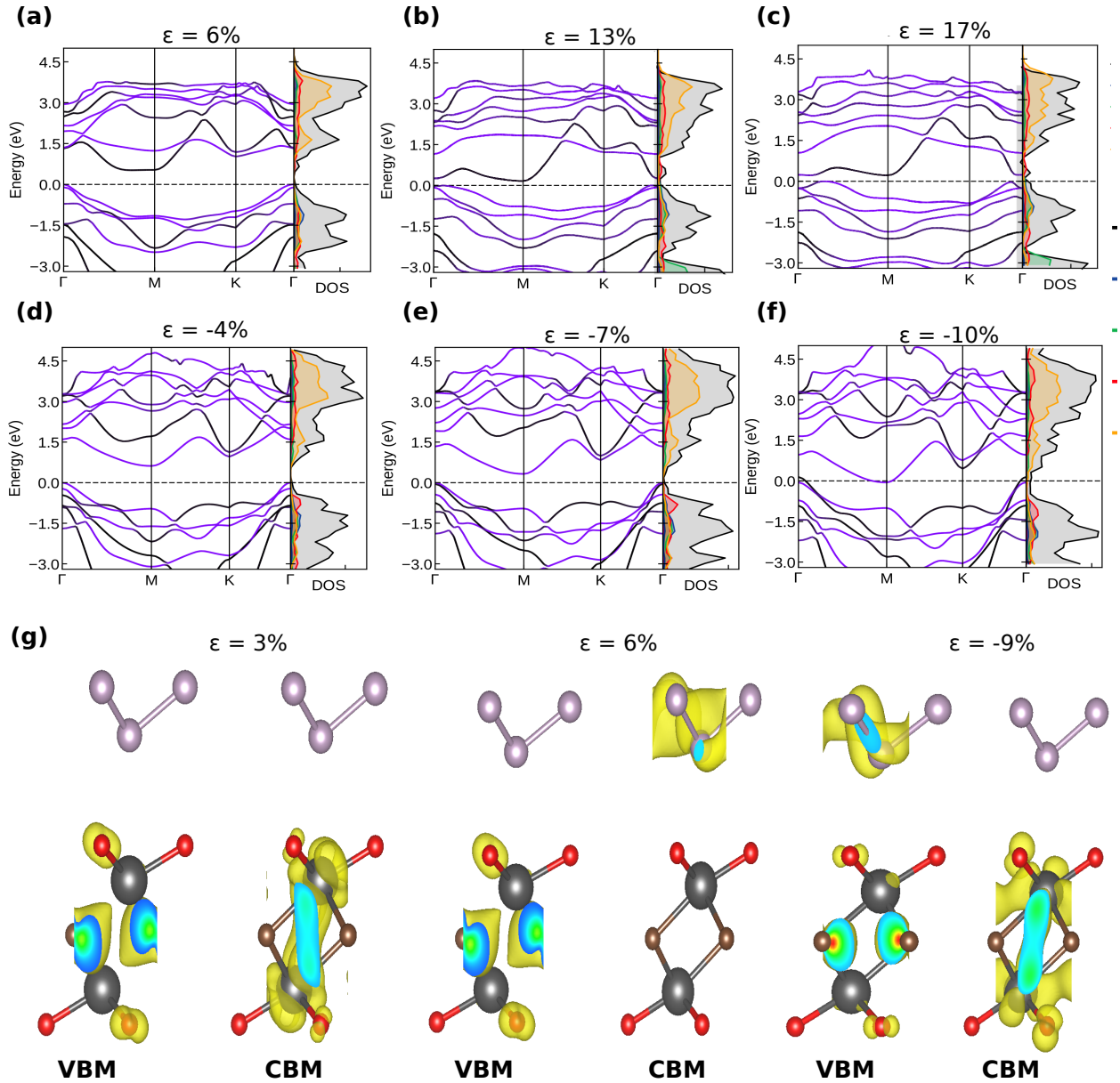


Figure 11: Band structures, PDOS [(a)-(f)] and (g) Band decomposed charge density of  $Zr_2CO_2/blueP$  heterostructures under different percentages of uniaxial strain along armchair direction

for -16%, the S-M transitions occur when CBM and VBM cross the Fermi level at K and  $\Gamma$  point. Similar changes in band structure were observed for strain applied along the zig-zag direction. Indirect to direct band gap transition at 6% strain and closing of band gap at for 12 % strain occurs under tensile strain. In the case of compressive strain, there is no major change occurs other than S-M transition at -16% strain. The change in band structure for

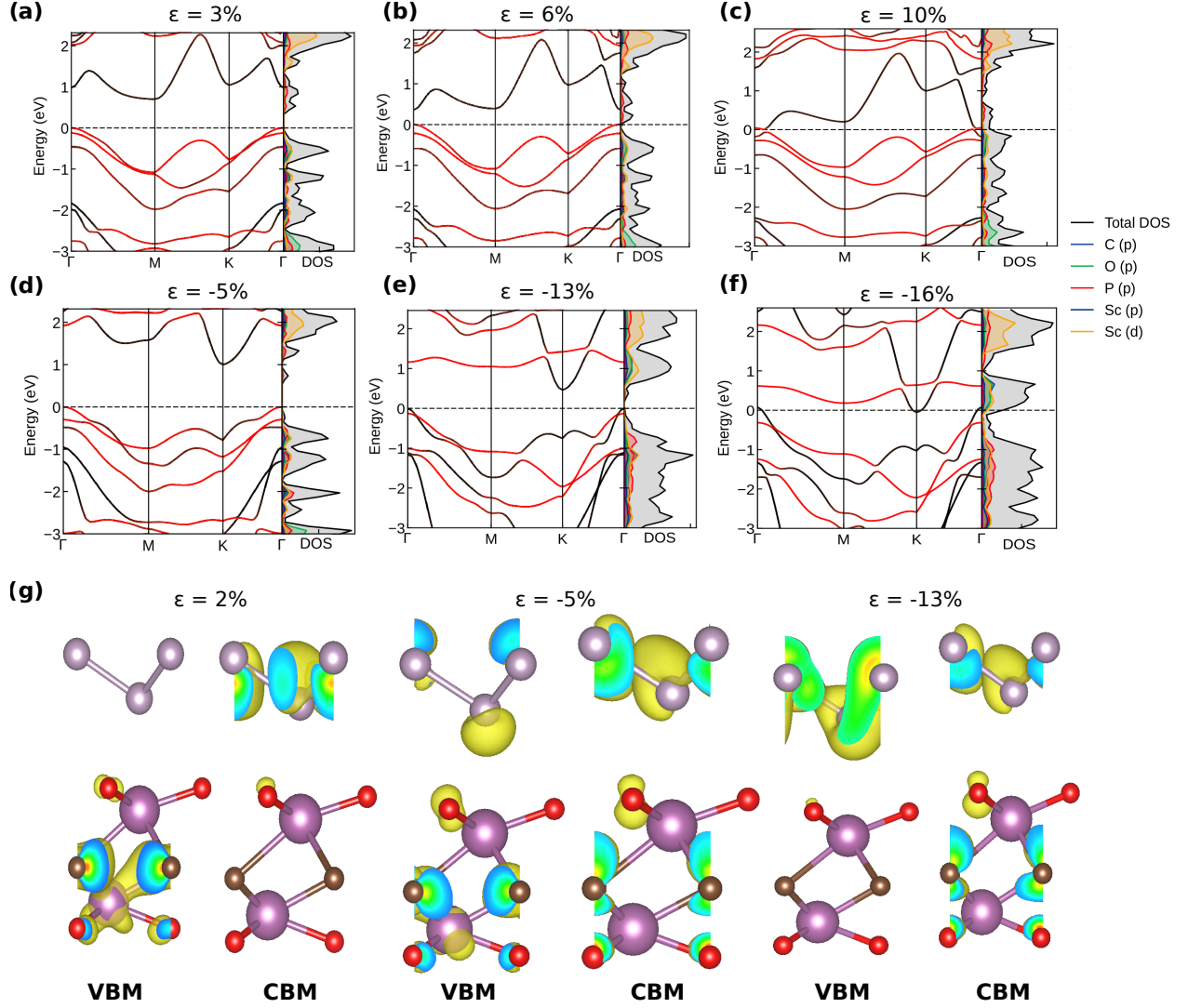


Figure 12: Band structures, PDOS [(a)-(f)] and (g) Band decomposed charge density of  $\text{Sc}_2\text{CO}_2/\text{blueP}$  heterostructures under different percentages of uniaxial strain along armchair direction

strain in the zig-zag direction is given in the Supporting Information (Figure S8).

**Normal compressive strain:** Next, we have studied the impact of normal compressive (NC) strain on the electronic properties of  $\text{M}_2\text{CO}_2/\text{blueP}$  heterostructures. The NC strain was determined as  $\epsilon = (l_0 - l)/l_0$ , where  $l_0$  and  $l$  are the un strained and strained layered distance (Figure 13 (b)), respectively. The interlayer distance is denoted by  $d$ . Figure 13 (a) shows the calculated band gap as a function of NC strain. Initially, we observe a slight increment in the band gap for small strain percentages, which is followed by a smooth

reduction as the strain increases. In contrast to other strains (biaxial, uniaxial), there is no S-M transition observed in all the considered heterostructures.

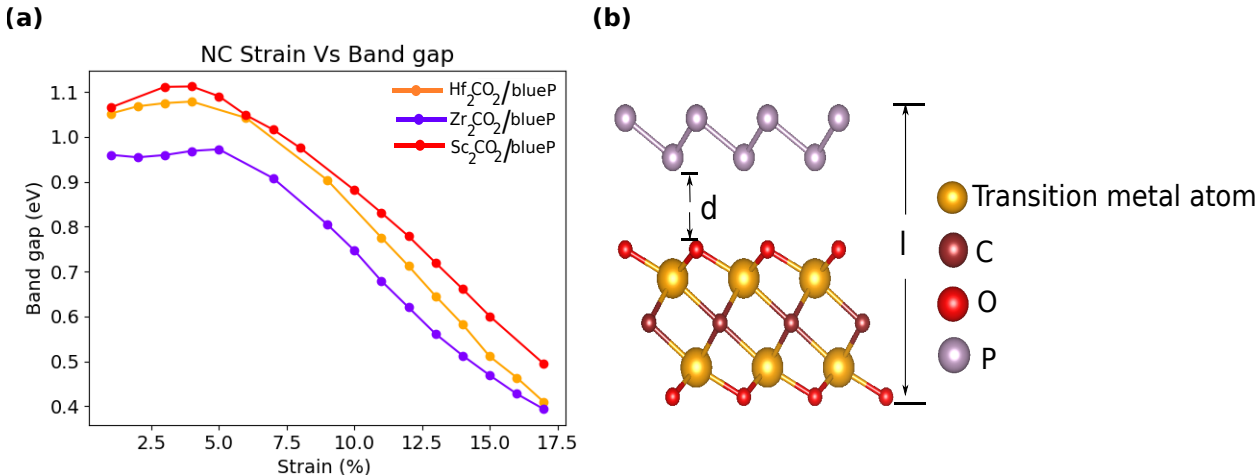


Figure 13: (a) The change in bandgaps of MXene/blueP heterostructures under various percentages of applied NC strain and (b) Schematic of NC strain ( $\text{Hf}(\text{Zr})_2\text{CO}_2/\text{blueP}$  heterostructure)

The impact of NC strain on the electronic structure of each heterostructure was analyzed, as depicted in Figure 14. The band structure calculations show a consistent downward shift of the CBM across all considered systems, while the position of VBM remains unaffected in  $\text{Hf}_2\text{CO}_2/\text{blueP}$  and  $\text{Zr}_2\text{CO}_2/\text{blueP}$  under normal compressive strain, a notable shift occurs in  $\text{Sc}_2\text{CO}_2/\text{blueP}$ , where the VBM transitions from  $\Gamma$  to in between  $\Gamma$  and M points. Similar to the other strains, the normal compressive strain also causes the type-I to type-II conversion in  $\text{Hf}_2\text{CO}_2/\text{blueP}$  (8%) and  $\text{Zr}_2\text{CO}_2/\text{blueP}$  (7%) vdW heterostructures. The band decomposed charge density plot for  $\text{M}_2\text{CO}_2/\text{blueP}$  ( $\text{M}=\text{Hf}, \text{Zr}, \text{Sc}$ ) is given in Figure 14 (j-l). In the  $\text{Hf}(\text{Zr})_2\text{CO}_2/\text{blueP}$  heterostructure, the band gap decreases due to the CBM shifting closer to the Fermi level. Additionally, in the case of  $\text{Sc}_2\text{CO}_2/\text{blueP}$  heterostructure, under increased strain, shifts occur both in the VBM and CBM. For the initial strain conditions, the CBM of the  $\text{Hf}(\text{Zr})_2\text{CO}_2/\text{blueP}$  heterostructure was primarily influenced by the  $\text{Hf}(\text{Zr})$ -d states, while VBM saw significant contributions from the C-p and O-p states. As the NCS increased, the involvement of the p states of P in the CBM intensified. At 8(7)% strain, the dominance of the P-p state in the CBM was evident, leading to a transition from type-I to type-II behavior

in the Hf(Zr)<sub>2</sub>CO<sub>2</sub>/blueP heterostructure. Conversely, in the Sc<sub>2</sub>CO<sub>2</sub>/blueP heterostructure, the CBM was largely governed by the p states of P, while the VBM saw notable contributions from the Sc-d, O(C)-p, and Sc-p states. With increasing strain, the participation of the p states of P in the VBM increased, although no dominance of these states was observed, and no type-II to type-I transition occurred.

### 3.4 Thermoelectric properties

Tuning of electronic properties of materials can influence their thermoelectric properties as these properties are closely related to the band structures. Utilizing band structures as previously computed, we have derived the electronic transport coefficients for all the heterostructures, encompassing the Seebeck coefficient (S), electrical conductivity ( $\sigma/\tau$ ), electronic contribution to thermal conductivity ( $\kappa_e/\tau$ ), power factor ( $S^2\sigma/\tau$ ) and the electronic figure of merit, denoted by  $ZT_e$ , defined as:

$$ZT_e = \frac{S^2\sigma T}{\kappa_e} \quad (8)$$

This equation encapsulates the attributes of electron transport and serves as an upper limit for the ZT value.<sup>62</sup> According to the proportionality,  $ZT_e$  can be maximized by increasing the numerator and decreasing the denominator. However, achieving this is complex due to the conflicting interdependencies among various coefficients. In high-temperature applications, thorough scrutiny of the influence of both power factor and thermal conductivity is essential, highlighting their paramount importance in such contexts.<sup>63</sup> Also, adjusting power factor (PF) has been demonstrated as a superior approach for enhancing efficiency and power generation compared to conventional methods of reducing lattice thermal conductivity, as it doesn't compromise thermo-mechanical stability.<sup>64</sup> We have explored the impact of doping charge carriers on these transport coefficients by adjusting the charge carrier concentrations. The negative and positive charge carrier concentrations correspond to electron (n-type) and

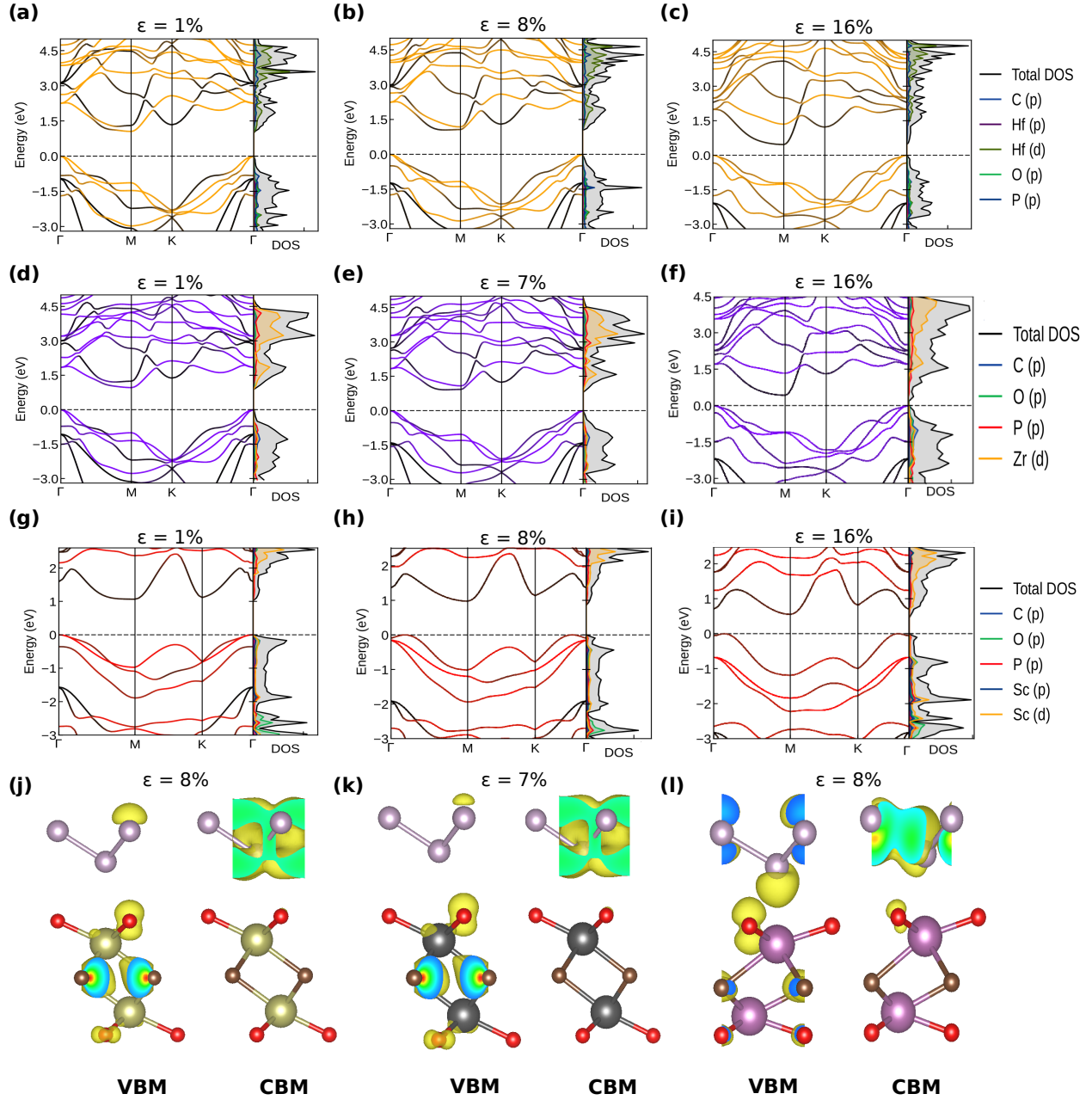


Figure 14: Band structures, PDOS of Hf<sub>2</sub>CO<sub>2</sub>/blueP [(a)-(c)], Zr<sub>2</sub>CO<sub>2</sub>/blueP [(d)-(f)], Sc<sub>2</sub>CO<sub>2</sub>/blueP [(g)-(i)] and band decomposed charge density of (j) Hf<sub>2</sub>CO<sub>2</sub>/blueP, (k) Zr<sub>2</sub>CO<sub>2</sub>/blueP, (l) Sc<sub>2</sub>CO<sub>2</sub>/blueP heterostructures, respectively under different percentage of NC strain

hole (p-type) doping, respectively.<sup>65</sup>

Seebeck coefficient, also referred to as thermopower, characterizes the electrical potential generated by a temperature gradient within a material. To achieve a high Seebeck coef-

efficient, symmetry breaking is desired, often manifested as a sharp peak in the DOS. This can be accomplished through band convergence via strain application or resonant doping.<sup>66</sup> Electrical conductivity, denoted as  $\sigma$ , characterizes the medium's ability to conduct current. High electrical conductivity is a desirable characteristic of efficient thermoelectric materials. Although the CSTA may oversimplify electrical transport phenomena, it provides a reasonable description of electrical conductivity, particularly under conditions such as doping of charge carriers or the application of external strain on the unit cell.<sup>38</sup> Electrical and thermal conductivities exhibit a proportional relationship as per Wiedemann-Franz law,<sup>67</sup> based on a simplistic free electron model. Considering the intricate interactions experienced by electrons due to atomic and electronic environments, there exists potential for optimizing the thermoelectric performance of materials. Herein, we systematically compute the electronic transport coefficients and their susceptibility to different strain conditions.

**Biaxial strain** : From the calculated seebeck coefficient, electrical conductivity, thermal conductivity, power factor and electronic figure of merit as shown in Figure 15, it can be inferred that, the thermal and electrical conductivity profiles of both  $\text{Hf}_2\text{CO}_2/\text{blueP}$  and  $\text{Zr}_2\text{CO}_2/\text{blueP}$  heterostructures exhibit notable similarities. In the case of p-type doping, positive strain induces a decrease in both conductivities, whereas negative strain results in an increase. In smaller doping concentration ranges, n-type doping largely has minimal effects on conductivities. However, as the doping concentration increases, significant changes in conductivity values become apparent. Comparing the Seebeck coefficients,  $\text{Hf}_2\text{CO}_2/\text{blueP}$  heterostructures demonstrate greater variability compared to  $\text{Zr}_2\text{CO}_2/\text{blueP}$  heterostructures, a trend also reflected in their respective  $ZT_e$  values.  $ZT_e$  reaches its maximum at zero strain for both heterostructures. Conversely, for the PF,  $\text{Zr}_2\text{CO}_2/\text{blueP}$  heterostructures demonstrate more variability than  $\text{Hf}_2\text{CO}_2/\text{blueP}$  when strain is introduced.  $\text{Sc}_2\text{CO}_2/\text{blueP}$  heterostructure also displays analogous patterns in the effects of positive and zero strain on conductivities. However, negative strain profoundly impacts the conductivities in both doping domains. The Seebeck coefficient peaks at negative strain values, corresponding to a

proportional increase in  $ZT_e$  values.

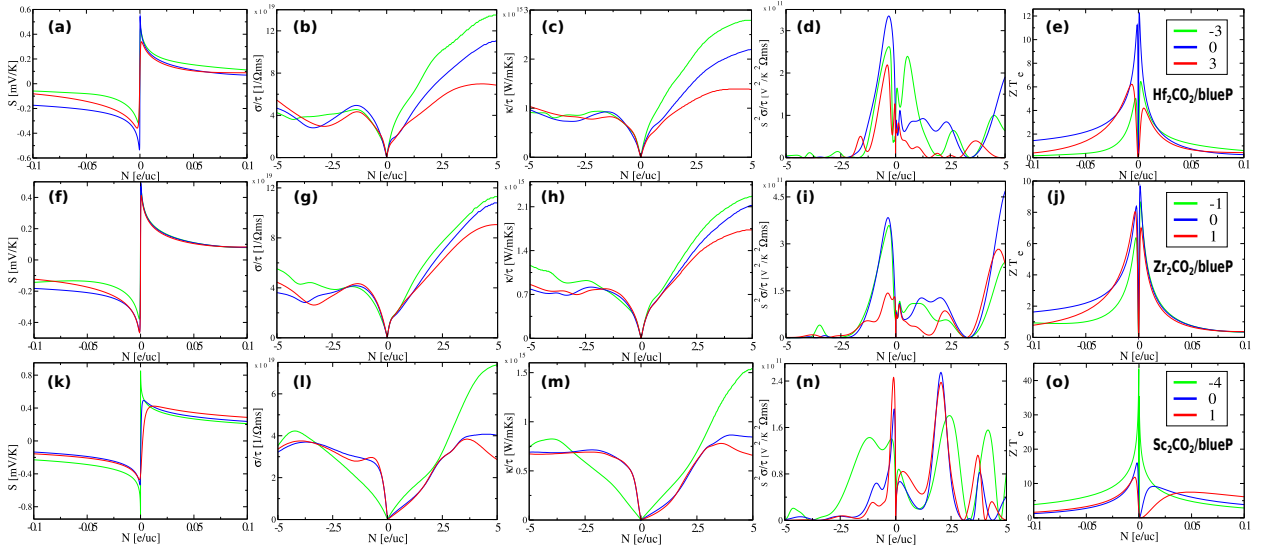


Figure 15: Calculated Seebeck coefficient, Electrical conductivity, Thermal conductivity, Power Factor and electronic Figure of Merit of  $\text{Hf}_2\text{CO}_2/\text{blueP}$  [(a)-(e)],  $\text{Zr}_2\text{CO}_2/\text{blueP}$  [(f)-(j)] and  $\text{Sc}_2\text{CO}_2/\text{blueP}$  [(k)-(o)] heterostructures respectively for different percentages of biaxial strain

### Uniaxial strain along zig-zag and armchair direction: Based on the calculated See-

beck coefficient, electrical conductivity, thermal conductivity, power factor, and electronic figure of merit presented in Figure 16, the following observations can be inferred. For all the heterostructures, armchair and zigzag strain exert no positive influence on the Seebeck coefficient, a pattern also evident in the  $ZT_e$  values. The maximum  $ZT_e$  values are observed with zero strain across all combinations of heterostructures. Both strains lead to a decrease in the Seebeck coefficient, with positive strain causing a more pronounced reduction compared to negative strain. This same trend is observed in the  $ZT_e$  values. Under negative armchair strain, both  $\text{Hf}_2\text{CO}_2/\text{blueP}$  and  $\text{Zr}_2\text{CO}_2/\text{blueP}$  heterostructure exhibit peaks around a charge carrier concentration of -2.5 in the conductivity plots, which correspondingly maximizes the power factor in the same regions. In the case of zigzag strain, while both strains decrease conductivities for both heterostructures in the p-type doping regions, they increase in the n-type regions. Significant discrepancies between positive and negative strain are ob-

served for  $\text{Zr}_2\text{CO}_2/\text{blueP}$  heterostructure in the n-type regions, whereas the profiles remain relatively similar for  $\text{Hf}_2\text{CO}_2/\text{blueP}$  heterostructure. This observation serves as the evident reason for the power factor peaking at different regions for different strains in  $\text{Zr}_2\text{CO}_2/\text{blueP}$  heterostructures, while the power factor peaks around zero doping areas for  $\text{Hf}_2\text{CO}_2/\text{blueP}$  heterostructures.

Armchair strain in  $\text{Sc}_2\text{CO}_2/\text{blueP}$  heterostructure significantly influences conductivities within the n-type doping domain, leading to a peak in the power factor around these areas for both strains. Similarly, zigzag strain also exerts a considerable impact on conductivities. However, positive strain induces substantial effects in conductivities, consequently maximizing the power factor.

**Normal Compressive strain:** We have examined the impact of NC strain on the transport coefficients of  $\text{M}_2\text{CO}_2/\text{blueP}$  heterostructures as shown in Figure 17. In all the heterostructures, strain exhibits a positive effect on both power factor and  $\text{ZT}_e$  values. Specifically in  $\text{Hf}_2\text{CO}_2/\text{blueP}$  heterostructure, at 3% strain, a significant disparity in the Seebeck coefficient and conductivity profiles emerges, leading to peaks in power factor and  $\text{ZT}_e$  values in the n-type domains. In  $\text{Zr}_2\text{CO}_2/\text{blueP}$  heterostructure, minimal changes are observed in all the Onsager coefficient plots, resulting in minimal impact on both power factor and  $\text{ZT}_e$ . The power factor peaks for zero strain, whereas  $\text{ZT}_e$  reaches its peak at 5% strain, where the Seebeck coefficient exhibits a slightly higher value compared to others. In  $\text{Sc}_2\text{CO}_2/\text{blueP}$  heterostructure, a significant increase in power factor is observed at 2% strain owing to a substantial rise in electrical conductivity. However, this leads to a decrease in  $\text{ZT}_e$  due to a corresponding increase in thermal conductivity. Conversely, at 9% strain, the higher Seebeck coefficient and lower thermal conductivity result in an enlarged  $\text{ZT}_e$  value.

The maximum PF,  $\text{ZT}_e$ , and band alignment type for all the heterostructures and their respective strain conditions are summarized in Table 2. The analysis indicates that negative biaxial strain has a profound effect on increasing the  $\text{ZT}_e$  values specifically for the

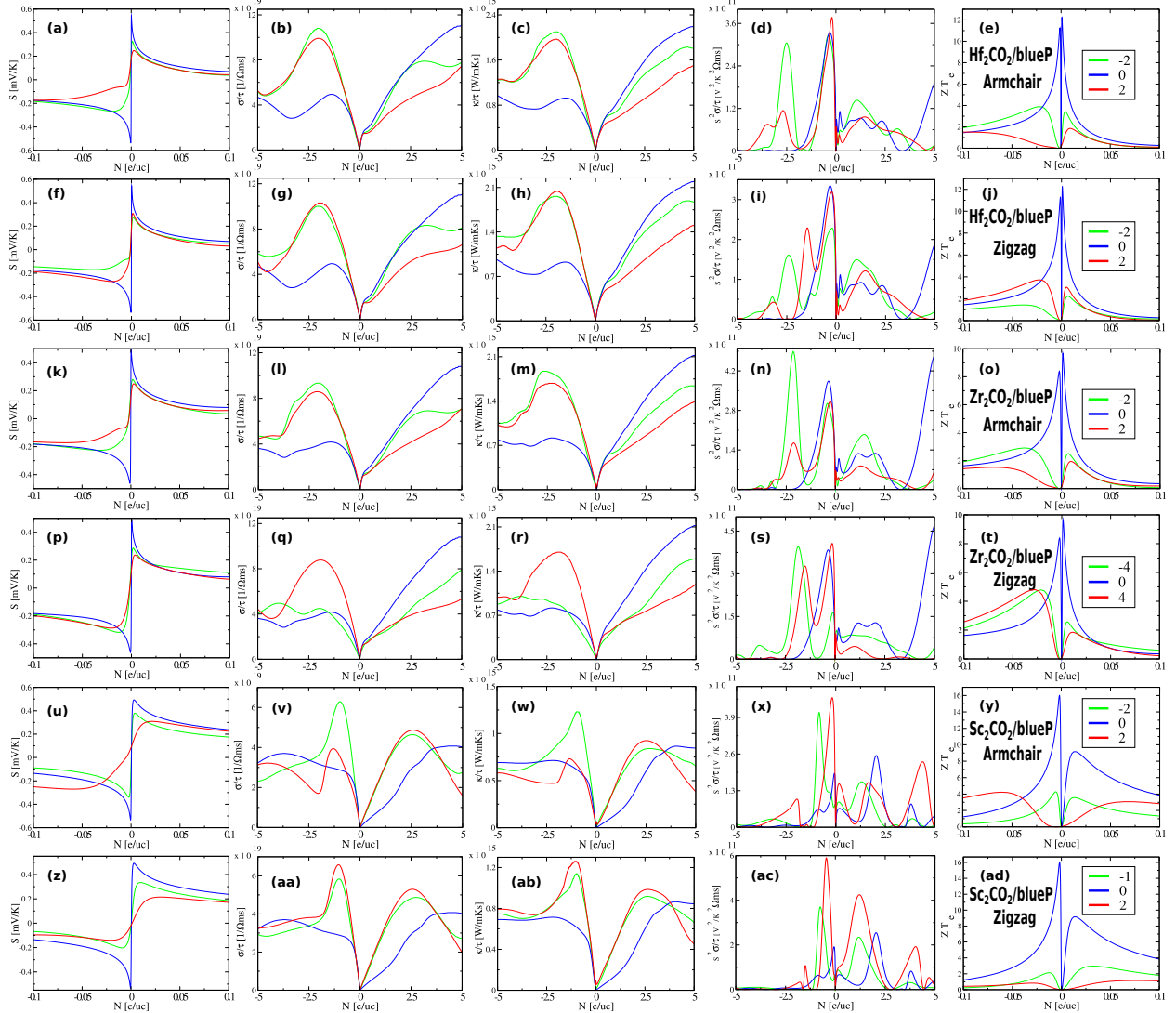


Figure 16: Calculated Seebeck coefficient, Electrical conductivity, Thermal conductivity, Power Factor and electronic Figure of Merit of  $\text{Hf}_2\text{CO}_2/\text{blueP}$  [Armchair (a)-(e), Zigzag (f)-(j)],  $\text{Zr}_2\text{CO}_2/\text{blueP}$  [Armchair (k)-(o), Zigzag (p)-(t)] and  $\text{Sc}_2\text{CO}_2/\text{blueP}$  [Armchair (u)-(y), Zigzag (z)-(ad)] respectively for different percentages of uniaxial strain

$\text{Zr}_2\text{CO}_2/\text{blueP}$  heterostructure, surpassing all other heterostructures and strain conditions. Conversely, uniaxial strain, whether armchair or zigzag, did not lead to  $ZT_e$  enhancement for any heterostructure. However, it did result in an increased power factor compared to the unstrained condition for all heterostructures except  $\text{Hf}_2\text{CO}_2/\text{blueP}$  in zigzag strain. Additionally, normal compressive strain notably doubled the power factor for  $\text{Hf}_2\text{CO}_2/\text{blueP}$  and increased it by over five times for  $\text{Sc}_2\text{CO}_2/\text{blueP}$ , marking the highest improvement

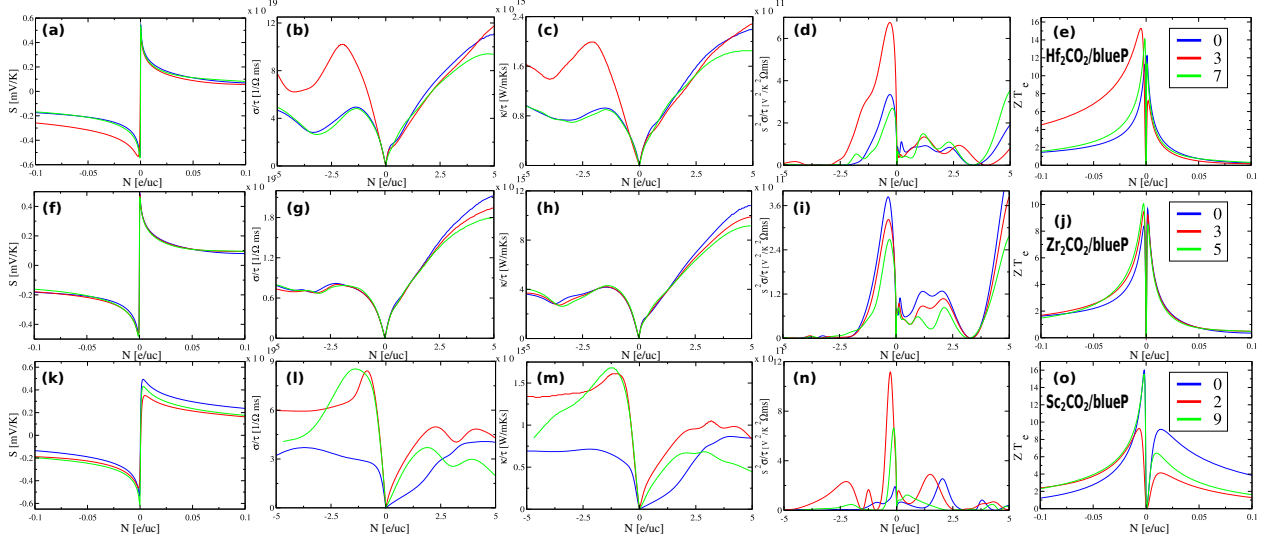


Figure 17: Calculated Seebeck coefficient, Electrical conductivity, Thermal conductivity, Power Factor and electronic Figure of Merit of  $\text{Hf}_2\text{CO}_2/\text{blueP}$  [(a)-(e)],  $\text{Zr}_2\text{CO}_2/\text{blueP}$  [(f)-(j)], and  $\text{Sc}_2\text{CO}_2/\text{blueP}$  [(k)-(o)] heterostructures respectively for different percentages of normal compressive strain

among all heterostructures and different strain conditions. Our power factor values exhibit comparability and occasionally surpass those documented for existing thermoelectric materials.<sup>68–70</sup> Although  $ZT_e$  values displayed some enhancement,  $\text{Sc}_2\text{CO}_2/\text{blueP}$  did not exhibit improvement in this aspect. In addition, we have provided band alignment diagrams to offer a clearer understanding of the band alignment types for both unstrained heterostructures and those under strain conditions where maximum PF and  $ZT_e$  values are achieved, as given in the supplementary materials (see Figure S9).

### 3.5 CONCLUSION

We conducted a systematic study on the geometric structure, stability, electronic properties and modulation of electronic and thermoelectric properties of  $\text{M}_2\text{CO}_2$  ( $\text{M} = \text{Hf}, \text{Zr}, \text{Sc}$ )/blueP heterostructures under biaxial and uniaxial strain.  $\text{Hf}_2\text{CO}_2/\text{blueP}$ ,  $\text{Zr}_2\text{CO}_2/\text{blueP}$  was observed to be type-I and  $\text{Sc}_2\text{CO}_2/\text{blueP}$  a type-II heterostructure with indirect band gaps of 1.04 eV, 0.95 eV, and 1.06 eV, respectively. Employing phonon dispersion and *ab initio* molecular dynamics (AIMD) calculations, we confirmed the dynamical and thermal stability

Table 2: Maximum PF,  $ZT_e$ , and band alignment type for all the heterostructures under different strain types and the corresponding strain values. The maximum obtained values of PF and  $ZT_e$  under strain has been indicated in bold for each heterostructure

Heterostructure	Type of strain	Max PF ( $\times 10^{11}$ W/mK <sup>2</sup> s)	Max $ZT_e$
Hf <sub>2</sub> CO <sub>2</sub> /blueP	Biaxial	3.4 ( $\epsilon = 0\%$ ) (type-I)	12.2 ( $\epsilon = 0\%$ ) (type-I)
	Uniaxial (Armchair)	3.8 ( $\epsilon = 2\%$ ) (type-I)	12.2 ( $\epsilon = 0\%$ ) (type-I)
	Uniaxial (Zigzag)	3.4 ( $\epsilon = 0\%$ ) (type-I)	12.2 ( $\epsilon = 0\%$ ) (type-I)
	Normal Compressive	<b>6.8</b> ( $\epsilon = 3\%$ ) (type-I)	<b>15.3</b> ( $\epsilon = 3\%$ ) (type-I)
Zr <sub>2</sub> CO <sub>2</sub> /blueP	Biaxial	3.8 ( $\epsilon = 0\%$ ) (type-I)	9.8 ( $\epsilon = 0\%$ ) (type-I)
	Uniaxial (Armchair)	<b>4.9</b> ( $\epsilon = -2\%$ ) (type-I)	9.8 ( $\epsilon = 0\%$ ) (type-I)
	Uniaxial (Zigzag)	4.1 ( $\epsilon = 4\%$ ) (type-I)	9.8 ( $\epsilon = 0\%$ ) (type-I)
	Normal Compressive	3.8 ( $\epsilon = 0\%$ ) (type-I)	<b>10.1</b> ( $\epsilon = 5\%$ ) (type-I)
Sc <sub>2</sub> CO <sub>2</sub> /blueP	Biaxial	2.6 ( $\epsilon = 0\%$ ) (type-II)	<b>43.2</b> ( $\epsilon = -4\%$ ) (type-II)
	Uniaxial (Armchair)	4.6 ( $\epsilon = 2\%$ ) (type-II)	16.0 ( $\epsilon = 0\%$ ) (type-II)
	Uniaxial (Zigzag)	5.9 ( $\epsilon = 2\%$ ) (type-II)	16.0 ( $\epsilon = 0\%$ ) (type-II)
	Normal Compressive	<b>11.2</b> ( $\epsilon = 2\%$ ) (type-II)	16.0 ( $\epsilon = 0\%$ ) (type-II)

of all the heterostructures considered. Additionally, our determination of the work function, derived from electrostatic potential calculations, demonstrated that the MXene components possess lower work functions than blueP.

Further investigation on strain engineering of these heterostructures revealed interesting modulation of electronic and thermoelectric properties such as, semiconductor to metal (S-M) transition, type-I to type-II conversion and enhanced PF and  $ZT_e$ . Hf<sub>2</sub>CO<sub>2</sub>/blueP and Zr<sub>2</sub>CO<sub>2</sub>/blueP show remarkable similarities under the application of strain. Both heterostructures demonstrate a discernible reduction in band gap with increasing compressive

and tensile biaxial strain, culminating in a S-M transition at -7% for both the heterostructures and at 18% and 14%, for  $Zr_2CO_2/blueP$  and  $Hf_2CO_2/blueP$ , respectively. In contrast,  $Sc_2CO_2/blueP$  shows an initial upward trend in band gap under low values of compressive strain, followed by a decrease, achieving an S-M transition at -10% strain. Under tensile strain, a sharp decrease in band gap is observed, with the heterostructure becoming metallic at 7% strain. We observed a type-I to type-II transition in both  $Hf_2CO_2/blueP$  and  $Zr_2CO_2/blueP$  under both tensile and compressive strain. Interestingly, we found a type-II to type-I transition in  $Sc_2CO_2/blueP$  at -7% strain, which shifts back to type-II at -8% strain. Applying uniaxial armchair strain to  $Hf(Zr)_2CO_2/blueP$  heterostructures did not close the band gap but induced a type I to type II transition, whereas zigzag strain induced both S-M and type I to type II transitions. For  $Sc_2CO_2/blueP$ , we observed an indirect-to-direct band gap transition under tensile strain for both armchair and zigzag orientations. We have observed S-M transition for both zigzag and arm chair under tensile and compressive strain. Notably, normal compressive (NC) strain did not induce a S-M transition but led to a gradual decrease in the band gap for large strain values. Similarly, as with other strains, a type I to type II transition was observed for  $Hf(Zr)_2CO_2/blueP$  heterostructures under NC strain.

In an extended study of strain engineering on thermoelectric properties, we observed a positive correlation between strain and power factor in the majority of strain conditions, whereby the electronic figure of merit is predominantly negatively affected under strain, with notable exceptions observed for biaxial strain, where its influence is substantial.  $Sc_2CO_2/blueP$  showed the highest  $ZT_e$  value of 43.2 at -4% biaxial strain among all the heterostructures. The maximum power factor ( $\times 10^{11}$  W/mK<sup>2</sup>s) obtained for  $Hf_2CO_2/blueP$ ,  $Zr_2CO_2/blueP$  and  $Sc_2CO_2/blueP$  are 6.8 ( at 3% NC strain), 4.9 (at -2% uniaxial armchair strain) and 11.2 (at 2% NC strain), respectively. We contend that the fine-tuning of the power factor holds paramount significance in high-temperature applications, and our discoveries are poised to be particularly valuable in this domain. These results highlight the potential of  $M_2CO_2/blueP$  heterostructures for electronic, optoelectronic and thermoelectric applications.

## CRediT authorship contribution statement

**Sarga P K (First Author):** Conceptualization, Data Curation, Methodology, Investigation, Formal Analysis, Writing - Original Draft, Review & Editing. **Karthik H J:** Investigation, Methodology, Data curation, Formal Analysis, Writing - Review & Editing. **Swastibrata Bhattacharyya (Corresponding Author):** Conceptualization, Methodology, Validation, Formal Analysis, Resources, Supervision, Writing - Review & Editing.

## Supporting Information Available

- Lattice parameter and bond lengths of all considered monolayers; Formation energy and Bader charge distribution in  $M_2CO_2$ /blueP heterostructure; Top and side views of the different stacking configurations of the  $M_2CO_2$ /blueP heterostructure; Elastic constants ( $C_{11}$ ,  $C_{12}$ ,  $C_{66}$ ), and Young's modulus( $Y$ ) of monolayers and heterostructures; Band structure, PDOS and Band decomposed charge density of  $Zr_2CO_2$ /blueP ( $Hf(Sc)_2CO_2$ /blueP) heterostructure under different percentages of biaxial (Zigzag and armchair) strain; Band alignment of  $M_2CO_2$ /blueP heterostructure for unstrained as well as strained values of maximum PF and ZT.

## Acknowledgement

SB acknowledges the financial support from the Science and Engineering Research Board (SERB), Government of India (grant numbers SRG/2020/000562, CRG/2020/000434 and CRG/2023/003688), and BITS Pilani K. K. Birla Goa Campus, India (grant numbers GOA/ACG/2019-20/NOV/08 and C1/23/211). SPK acknowledges the financial support from SERB, Government of India (grant number SRG/2020/000562). All authors acknowledge the High-Performance Computing Facility (HPC) at BITS Pilani K. K. Birla Goa Campus.

## Data availability

Data will be made available on request.

## References

- (1) Geim, A. K.; Novoselov, K. S. The rise of graphene. Nat. Mater. **2007**, 6, 183–191.
- (2) Liu, S.; Pan, X.; Liu, H. Two-dimensional nanomaterials for photothermal therapy. Angew. Chem. **2020**, 132, 5943–5953.
- (3) Pomerantseva, E.; Gogotsi, Y. Two-dimensional heterostructures for energy storage. Nat. Energy. **2017**, 2, 1–6.
- (4) Naguib, M.; Mashtalir, O.; Carle, J.; Presser, V.; Lu, J.; Hultman, L.; Gogotsi, Y.; Barsoum, M. W. Two-dimensional transition metal carbides. ACS Nano **2012**, 6, 1322–1331.
- (5) Naguib, M.; Mochalin, V. N.; Barsoum, M. W.; Gogotsi, Y. 25th anniversary article: MXenes: a new family of two-dimensional materials. Adv. Mater. **2014**, 26, 992–1005.
- (6) Anasori, B.; Xie, Y.; Beidaghi, M.; Lu, J.; Hosler, B. C.; Hultman, L.; Kent, P. R.; Gogotsi, Y.; Barsoum, M. W. Two-dimensional, ordered, double transition metals carbides (MXenes). ACS Nano **2015**, 9, 9507–9516.
- (7) Naguib, M.; Kurtoglu, M.; Presser, V.; Lu, J.; Niu, J.; Heon, M.; Hultman, L.; Gogotsi, Y.; Barsoum, M. W. Two-dimensional nanocrystals produced by exfoliation of  $\text{Ti}_3\text{AlC}_2$ . Adv. Mater. **2011**, 23, 4248–4253.
- (8) Lee, Y.; Cho, S. B.; Chung, Y.-C. Tunable indirect to direct band gap transition of monolayer  $\text{Sc}_2\text{CO}_2$  by the strain effect. ACS Appl. Mater. Interfaces. **2014**, 6, 14724–14728.

- (9) Khazaei, M.; Arai, M.; Sasaki, T.; Chung, C.-Y.; Venkataramanan, N. S.; Estili, M.; Sakka, Y.; Kawazoe, Y. Novel electronic and magnetic properties of two-dimensional transition metal carbides and nitrides. Adv. Funct. Mater. **2013**, 23, 2185–2192.
- (10) Geim, A. K.; Grigorieva, I. V. Van der Waals heterostructures. Nature **2013**, 499, 419–425.
- (11) Roy, T.; Tosun, M.; Cao, X.; Fang, H.; Lien, D.-H.; Zhao, P.; Chen, Y.-Z.; Chueh, Y.-L.; Guo, J.; Javey, A. Dual-gated MoS<sub>2</sub>/WSe<sub>2</sub> van der Waals tunnel diodes and transistors. ACS Nano **2015**, 9, 2071–2079.
- (12) Lopez-Sanchez, O.; Alarcon Llado, E.; Koman, V.; Fontcuberta i Morral, A.; Radenovic, A.; Kis, A. Light generation and harvesting in a van der Waals heterostructure. ACS Nano **2014**, 8, 3042–3048.
- (13) Huo, N.; Kang, J.; Wei, Z.; Li, S.-S.; Li, J.; Wei, S.-H. Novel and enhanced optoelectronic performances of multilayer MoS<sub>2</sub>–WS<sub>2</sub> heterostructure transistors. Adv. Funct. Mater. **2014**, 24, 7025–7031.
- (14) Marschall, R. Semiconductor composites: strategies for enhancing charge carrier separation to improve photocatalytic activity. Adv. Funct. Mater. **2014**, 24, 2421–2440.
- (15) Özçelik, V. O.; Azadani, J. G.; Yang, C.; Koester, S. J.; Low, T. Band alignment of two-dimensional semiconductors for designing heterostructures with momentum space matching. Phys. Rev. B **2016**, 94, 035125.
- (16) Deng, D. K. s. novoselov, q. Fu, n. zheng, z. tian and X. Bao, Catalysis with two-dimensional materials and their heterostructures. Nat. Nanotechnol **2016**, 11, 218–230.
- (17) Novoselov, K.; Mishchenko, A.; Carvalho, A.; Castro Neto, A. 2D materials and van der Waals heterostructures. Science **2016**, 353, aac9439.

- (18) Ceballos, F.; Bellus, M. Z.; Chiu, H.-Y.; Zhao, H. Ultrafast charge separation and indirect exciton formation in a MoS<sub>2</sub>-MoSe<sub>2</sub> van der Waals heterostructure. ACS Nano **2014**, 8, 12717–12724.
- (19) Arora, A.; Nayak, P. K.; Bhattacharyya, S.; Maity, N.; Singh, A. K.; Krishnan, A.; Rao, M. R. Interlayer excitonic states in MoSe<sub>2</sub>/MoS<sub>2</sub> van der Waals heterostructures. Phys. Rev. B **2021**, 103, 205406.
- (20) Kang, J.; Tongay, S.; Zhou, J.; Li, J.; Wu, J. Band offsets and heterostructures of two-dimensional semiconductors. Appl. Phys. Lett. **2013**, 102, 012111.
- (21) Wei, X.-L.; Zhang, H.; Guo, G.-C.; Li, X.-B.; Lau, W.-M.; Liu, L.-M. Modulating the atomic and electronic structures through alloying and heterostructure of single-layer MoS<sub>2</sub>. J. Mater. Chem. A **2014**, 2, 2101–2109.
- (22) Peng, Q.; Wang, Z.; Sa, B.; Wu, B.; Sun, Z. Electronic structures and enhanced optical properties of blue phosphorene/transition metal dichalcogenides van der Waals heterostructures. Sci. Rep. **2016**, 6, 31994.
- (23) Xu, L.; Wu, T.; Kent, P. R.; Jiang, D.-e. Interfacial charge transfer and interaction in the MXene/TiO<sub>2</sub> heterostructures. Phys. Rev. Mater **2021**, 5, 054007.
- (24) Du, Y.-T.; Kan, X.; Yang, F.; Gan, L.-Y.; Schwingenschlögl, U. MXene/graphene heterostructures as high-performance electrodes for Li-ion batteries. ACS Applied Materials & Interfaces **2018**, 10, 32867–32873.
- (25) Zhou, Q.; Wang, L.; Ju, W.; Yong, Y.; Wu, S.; Wang, Y.; Miao, H. A DFT study of Zr<sub>2</sub>CO<sub>2</sub>/MoS<sub>2</sub> heterostructures as gas sensors to HCN. Colloids Surf.A **2023**, 673, 131870.
- (26) Li, B.; Ren, C.-C.; Zhang, S.-F.; Ji, W.-X.; Zhang, C.-W.; Li, P.; Wang, P.-J. Electronic

- structural and optical properties of multilayer blue phosphorus: a first-principle study. J. Nanomater. **2019**, 2019, 4020762.
- (27) Ding, Y.; Wang, Y. Structural, electronic, and magnetic properties of adatom adsorptions on black and blue phosphorene: a first-principles study. J. Phys. Chem. C **2015**, 119, 10610–10622.
- (28) Li, Q.-F.; Duan, C.-G.; Wan, X.; Kuo, J.-L. Theoretical prediction of anode materials in Li-ion batteries on layered black and blue phosphorus. J. Phys. Chem. C **2015**, 119, 8662–8670.
- (29) Li, X.-H.; Wang, B.-J.; Wang, G.-D.; Ke, S.-H. Blue phosphorene/Sc<sub>2</sub>CX<sub>2</sub> (X = O, F) van der Waals heterostructures as suitable candidates for water-splitting photocatalysts and solar cells. Sustainable Energy Fuels **2020**, 4, 5277–5283.
- (30) Yuan, X.; Zhang, Z.; He, Y.; Zhao, S.; Zhou, N. Multilayer Load and Fast Diffusion of Metal Ions on a Ti<sub>2</sub>CS<sub>2</sub>/Blue Phosphorene Heterostructure Anode. J. Phys. Chem. C **2022**, 126, 91–101.
- (31) Rehman, G.; Ali Khan, S.; Ali, R.; Ahmad, I.; Gan, L.-Y.; Amin, B. Van der Waals heterostructures of blue phosphorene and scandium-based MXenes monolayers. J. Appl. Phys. **2019**, 126, 143101.
- (32) Guo, Z.; Miao, N.; Zhou, J.; Sa, B.; Sun, Z. Strain-mediated type-I/type-II transition in MXene/Blue phosphorene van der Waals heterostructures for flexible optical/electronic devices. J. Mater. Chem. C **2017**, 5, 978–984.
- (33) Huang, X.; Shu, X.; Li, J.; Cui, Z.; Cao, S.; Chen, W.; Yin, J.; Yan, G.; Zhao, H.; Hu, J.; others DFT study on type-II photocatalyst for overall water splitting: g-GaN/C<sub>2</sub>N van der Waals heterostructure. International Journal of Hydrogen Energy **2023**, 48, 12364–12373.

- (34) Zhu, Q.; Wang, S.; Wang, X.; Suwardi, A.; Chua, M. H.; Soo, X. Y. D.; Xu, J. Bottom-up engineering strategies for high-performance thermoelectric materials. Nanomicro Lett. **2021**, 13, 119.
- (35) Zhao, Y.; Zheng, M.; Wu, J.; Guan, X.; Suwardi, A.; Li, Y.; Lal, M.; Xie, G.; Zhang, G.; Zhang, L.; others Modification of thermal transport in few-layer MoS<sub>2</sub> by atomic-level defect engineering. Nanoscale **2021**, 13, 11561–11567.
- (36) Jia, N.; Cao, J.; Tan, X. Y.; Zheng, J.; Chien, S. W.; Yang, L.; Chen, K.; Ng, H. K.; Duran, S. S. F.; Liu, H.; others Suppressing Ge-vacancies to achieve high single-leg efficiency in GeTe with an ultra-high room temperature power factor. J. Mater. Chem. A **2021**, 9, 23335–23344.
- (37) Hong, S.; Gu, Y.; Seo, J. K.; Wang, J.; Liu, P.; Meng, Y. S.; Xu, S.; Chen, R. Wearable thermoelectrics for personalized thermoregulation. Sci. Adv. **2019**, 5, eaaw0536.
- (38) Kumari, A.; Nag, A.; Kumar, J. Strain engineering and thermoelectric performance of Janus monolayers of titanium dichalcogenides: A DFT study. Comput. Mater. Sci. **2023**, 218, 111925.
- (39) Sun, Y.; Abbas, A.; Wang, H.; Tan, C.; Li, Z.; Zong, Y.; Sun, H.; Wang, C.; Wang, H. Enhancement of thermoelectric performance of Cu<sub>2</sub>MnSnSe<sub>4</sub> alloys by regulation of lattice strain. J. Chem. Eng. **2024**, 150158.
- (40) Abid, A.; Idrees, M.; Din, H. U.; Alam, Q.; Amin, B.; Haneef, M. Structural, electronic, optical, thermoelectric and photocatalytic properties of SiS/MXenes van der Waals heterostructures. Mater. Today Commun. **2021**, 26, 101702.
- (41) Liu, Z.; Morales-Ferreiro, J.; Luo, T. First-principles study of thermoelectric properties of blue phosphorene. Applied Physics Letters **2018**, 113.

- (42) Kresse, G.; Joubert, D. From ultrasoft pseudopotentials to the projector augmented-wave method. Phys. Rev. B **1999**, 59, 1758.
- (43) Perdew, J. P.; Burke, K.; Ernzerhof, M. Generalized gradient approximation made simple. Phys. Rev. Lett. **1996**, 77, 3865.
- (44) Kresse, G.; Furthmüller, J. Efficient iterative schemes for ab initio total-energy calculations using a plane-wave basis set. Phys. Rev. B **1996**, 54, 11169.
- (45) Klimeš, J.; Bowler, D. R.; Michaelides, A. Van der Waals density functionals applied to solids. Phys. Rev. B **2011**, 83, 195131.
- (46) Togo, A.; Tanaka, I. First principles phonon calculations in materials science. Scr. Mater. **2015**, 108, 1–5.
- (47) Baroni, S.; Giannozzi, P.; Testa, A. Green’s-function approach to linear response in solids. Phys. Rev. Lett. **1987**, 58, 1861–1864.
- (48) Hedin, L. New Method for Calculating the One-Particle Green’s Function with Application to the Electron-Gas Problem. Phys. Rev. **1965**, 139, A796–A823.
- (49) Car, R.; Parrinello, M. Unified approach for molecular dynamics and density-functional theory. Phys. Rev. Lett. **1985**, 55, 2471.
- (50) Evans, D. J.; Holian, B. L. The nose–hoover thermostat. J. Chem. Phys. **1985**, 83, 4069–4074.
- (51) Ganose, A. M.; Jackson, A. J.; Scanlon, D. O. sumo: Command-line tools for plotting and analysis of periodic\* ab initio\* calculations. Journal of Open Source Software **2018**, 3, 717.
- (52) Momma, K.; Izumi, F. VESTA 3 for three-dimensional visualization of crystal, volumetric and morphology data. J. Appl. Crystallogr. **2011**, 44, 1272–1276.

- (53) Madsen, G. K. H.; Carrete, J.; Verstraete, M. J. BoltzTraP2, a program for interpolating band structures and calculating semi-classical transport coefficients. Comput. Phys. Commun. **2018**, 231, 140 – 145.
- (54) Gandi, A. N.; Alshareef, H. N.; Schwingenschlögl, U. Thermoelectric performance of the MXenes  $M_2CO_2$  ( $M = Ti, Zr, \text{ or } Hf$ ). Chemistry of Materials **2016**, 28, 1647–1652..
- (55) Li, X.-H.; Wang, B.-J.; Wang, G.-D.; Ke, S.-H. Blue phosphorene/ $Sc_2CX_2$  ( $X = O, F$ ) van der Waals heterostructures as suitable candidates for water-splitting photocatalysts and solar cells. Sustainable Energy Fuels **2020**, 4, 5277–5283.
- (56) Singh, S.; Romero, A. H. Giant tunable Rashba spin splitting in a two-dimensional BiSb monolayer and in BiSb/AlN heterostructures. Phys. Rev. B **2017**, 95, 165444.
- (57) Nosé, S. A unified formulation of the constant temperature molecular dynamics methods. J. Chem. Phys. **1984**, 81, 511–519.
- (58) Gao, C.; Singh, C. V. Mechanical properties and magnetic and electronic properties tuned via strain in two-dimensional non-van der Waals hematene. Nuclear Analysis **2023**, 2, 100061.
- (59) Lee, Y.; Hwang, Y.; Cho, S. B.; Chung, Y.-C. Achieving a direct band gap in oxygen functionalized-monolayer scandium carbide by applying an electric field. Phys. Chem. Chem. Phys. **2014**, 16, 26273–26278.
- (60) Li, J.; Shan, Z.; Ma, E. Elastic strain engineering for unprecedented materials properties. MRS Bull. **2014**, 39, 108–114.
- (61) He, K.; Poole, C.; Mak, K. F.; Shan, J. Experimental demonstration of continuous electronic structure tuning via strain in atomically thin  $MoS_2$ . Nano Lett. **2013**, 13, 2931–2936.

- (62) Mishra, P.; Singh, D.; Sonvane, Y.; Ahuja, R. Two-dimensional boron monochalcogenide monolayer for thermoelectric material. Sustainable Energy Fuels **2020**, 4, 2363–2369.
- (63) Wolf, M.; Hinterding, R.; Feldhoff, A. High power factor vs. high  $zT$ —A review of thermoelectric materials for high-temperature application. Entropy **2019**, 21, 1058.
- (64) Liu, W.; Kim, H. S.; Jie, Q.; Ren, Z. Importance of high power factor in thermoelectric materials for power generation application: A perspective. Scr. Mater. **2016**, 111, 3–9.
- (65) Fecher, G. H.; Rausch, E.; Balke, B.; Weidenkaff, A.; Felser, C. Half-Heusler materials as model systems for phase-separated thermoelectrics. Phys. Status Solidi (a) **2016**, 213, 716–731.
- (66) Lim, W. Y. S.; Zhang, D.; Duran, S. S. F.; Tan, X. Y.; Tan, C. K. I.; Xu, J.; Suwardi, A. Physical Intuition to Improve Electronic Properties of Thermoelectrics. Front. Phys. **2021**, 9, 755597.
- (67) Jones, W.; March, N. H. Theoretical solid state physics; Courier Corporation, 1985; Vol. 35.
- (68) Das, C.; Betal, A.; Alam, M.; Bera, J.; Gandi, A. N.; Sahu, S. Thermoelectric performance and optoelectronic properties of Janus monolayer of  $ZrXY$  ( $X= O, S$ )( $Y= S, Se$ ). Comput. Mater. Sci. **2023**, 218, 111993.
- (69) Ismail, K.; Murtaza, G.; Tahir, S.; Nazir, G.; Kattan, N. A.; Albalawi, H.; Haq, B. U.; Morsi, M. Theoretical study of electronic, magnetic, optical and thermoelectric properties of  $XMnO_2$  ( $X= Au, Ag, Cu$ ) oxides by DFT. J. Solid State Chem. **2022**, 314, 123432.
- (70) Bu, J.; Yang, X.; Ge, G.; Yang, G.; Yang, J. DFT insights on the electronic and thermoelectric properties of  $CuGaTe_2$  under pressure. Solid State Commun. **2022**, 352, 114836.